



# ALMA Resolves the First Strongly Lensed Optical/Near-IR-dark Galaxy

Marika Giulietti<sup>1,2</sup> , Andrea Lapi<sup>1,3,4,5</sup> , Marcella Massardi<sup>1,5,6</sup> , Meriem Behiri<sup>1</sup> , Martina Torsello<sup>1</sup> ,  
Quirino D'Amato<sup>1,2</sup> , Tommaso Ronconi<sup>1,4,7</sup> , Francesca Perrotta<sup>1</sup> , and Alessandro Bressan<sup>1</sup>

<sup>1</sup>SISSA, Via Bonomea 265, I-34136 Trieste, Italy; [mgiuliet@sissa.it](mailto:mgiuliet@sissa.it)

<sup>2</sup>INAF - Osservatorio di Astrofisica e Scienza dello Spazio, Via Gobetti 93/3, I-40129 Bologna, Italy

<sup>3</sup>IFPU - Institute for fundamental physics of the Universe, Via Beirut 2, I-34014 Trieste, Italy

<sup>4</sup>INFN-Sezione di Trieste, via Valerio 2, I-34127 Trieste, Italy

<sup>5</sup>INAF/IRA, Istituto di Radioastronomia, Via Piero Gobetti 101, I-40129 Bologna, Italy

<sup>6</sup>INAF, Istituto di Radioastronomia - Italian ARC, Via Piero Gobetti 101, I-40129 Bologna, Italy

<sup>7</sup>IFPU, Via Beirut 2, I-34014 Trieste, Italy

Received 2022 June 29; revised 2022 November 11; accepted 2022 November 21; published 2023 February 3

## Abstract

We present high-resolution ( $\lesssim 0''.1$ ) Atacama Large Millimeter/submillimeter Array observations of the strongly lensed galaxy HATLASJ113526.2-01460 at redshift  $z \sim 3.1$ , discovered in the GAMA 12th field of the Herschel-ATLAS survey. This gravitationally lensed system is remarkably peculiar, in that neither the background source nor the foreground lens show a clearly detected optical/near-IR Hubble Space Telescope-J band emission. We perform accurate lens modeling and source morphology reconstruction in three different (sub)millimeter continuum bands and in the C[II] and CO(8–7) spectral lines. The modeling indicates a foreground lensing (likely elliptical) galaxy with mass  $\gtrsim 10^{11} M_{\odot}$  at  $z \gtrsim 1.5$ , while the source (sub)millimeter continuum and line emissions are amplified by factors  $\mu \sim 6$ –13. We estimate extremely compact sizes— $\lesssim 0.5$  kpc for the star-forming region and  $\lesssim 1$  kpc for the gas component—with no clear evidence of rotation or ongoing merging events. We perform broadband SED fitting and retrieve the intrinsic demagnified physical properties of the source, which is found to feature a very high star formation rate,  $\gtrsim 10^3 M_{\odot} \text{ yr}^{-1}$ , which, given the compact sizes, is on the verge of the Eddington limit for starbursts; the radio luminosity at 6 cm from the available EVLA observations is consistent with star formation activity. The galaxy is found to be extremely rich in gas  $\sim 10^{11} M_{\odot}$  and dust  $\gtrsim 10^9 M_{\odot}$ . The stellar content  $\lesssim 10^{11} M_{\odot}$  places the source well above the main sequence of star-forming galaxies, indicating that the starburst is rather young, with an estimated age  $\sim 10^8$  yr. Our results indicate that the overall properties of HATLASJ113526.2-01460 are consistently explained by in situ galaxy formation and evolution scenarios.

*Unified Astronomy Thesaurus concepts:* [Strong gravitational lensing \(1643\)](#); [High-redshift galaxies \(734\)](#); [Galaxy formation \(595\)](#); [Submillimeter astronomy \(1647\)](#)

## 1. Introduction

Submillimeter galaxies (SMGs) are the main protagonists of star formation at early cosmic times (Blain 1996; Casey et al. 2014). It is well established that a substantial contribution at the peak of the cosmic star formation rate (SFR) density comes from these heavily dust-obscured objects, featuring a submillimeter (submm) flux density  $S_{870\mu\text{m}} \gtrsim 1$  mJy and extremely high SFRs, up to  $\sim 10^3 M_{\odot} \text{ yr}^{-1}$  (e.g., Dudzevičiūtė 2020; Simpson et al. 2020). Because of their huge dust content, these objects are heavily obscured in optical bands and extremely bright in far-IR (FIR)/submm bands, where the light of newborn stars, reprocessed by dust, is re-emitted. Moreover, SMGs have been identified as the progenitors of massive quiescent early-type galaxies, and constitute ideal laboratories for testing galaxy evolutionary models. For example, in in situ coevolutionary scenarios (Lapi et al. 2014, 2018; Pantoni et al. 2019), the intense star formation activity is accompanied by the exponential growth of the active nucleus, whose feedback will eventually sweep away the interstellar medium (ISM). The star formation is thus stopped on a relatively short timescale, while the nucleus shines as an optical quasar.

In recent years, an even more extreme population of heavily obscured SMGs has been discovered. These objects are missed in optical/near-IR (NIR) surveys, and they have been found up to very high redshifts ( $z \sim 6$ ; Riechers et al. 2013; Marrone et al. 2018; Riechers et al. 2020). These heavily obscured star-forming galaxies often lack a counterpart, even in deep-NIR observed-frame Hubble Space Telescope (HST) images (Alcalde Pampliega et al. 2019; Wang et al. 2019; Gruppioni et al. 2020), or they show extreme red colors ( $H-3.6 \mu\text{m} > 4$ ; see, e.g., Wang et al. 2016) and are only visible in observed-frame mid-IR (MIR) images performed by, e.g., the Spitzer/Infrared Array Camera (IRAC). Samples of optical/NIR-dark objects have been detected by observing deep CO line emissions (Riechers et al. 2020), and they have been efficiently selected in sensitive radio observations (Talia et al. 2021; Enia et al. 2022). These peculiar objects provide a significant and previously unknown contribution to the cosmic SFR density at  $z \gtrsim 3$ , estimated to be at least 10% up to 25%–40% of the one inferred from UV-selected populations (Wang et al. 2019; Williams et al. 2019; Gruppioni et al. 2020; Talia et al. 2021; Enia et al. 2022).

However, the studies that have been conducted so far have been limited by poor angular resolution and sensitivity in the MIR/FIR and submm bands, which has caused confusing problems and prohibited a detailed investigation of the physical properties of optical/NIR-dark galaxies and the conditions of their ISMs. In the last few years, Atacama Large Millimeter/

submillimeter Array (ALMA) deep-field observations have strongly improved the quality of observations of high-redshift dusty galaxies, detecting SMGs up to flux density limits of  $S_{870\mu\text{m}} \sim 0.1\text{--}1$  mJy (Aravena et al. 2016; Walter et al. 2016; Dunlop et al. 2017; Franco et al. 2018; Hatsukade et al. 2018), and have been crucial to establishing the physical properties of these bright sources ( $S_{870\mu\text{m}} > 1\text{--}2$  mJy), typically found at  $z \sim 2.5\text{--}3.0$  (e.g., Simpson et al. 2014, 2017; Dudzevičiūtė 2020; Simpson et al. 2020). However, even high-angular resolution studies indicate that these objects are extremely compact, with typical intrinsic sizes of a few tenths of an arcsecond (e.g., Ikarashi et al. 2015, 2017; Massardi et al. 2018; Pantoni et al. 2021), making them very hard to resolve.

Gravitational lensing enables the observation of regions in the luminosity–redshift spaces of these sources, which would otherwise be unattainable with the current instrumentation at reasonable integration times. The gravitational magnification of the foreground lens increases the apparent luminosity in proportion to the magnification  $\mu$  and stretches the angular sizes by a factor  $\sqrt{\mu}$ . This behavior offers the unique possibility of studying, down to subkiloparsec scales, the properties of objects that are not otherwise exceptionally bright, massive, or peculiar, and that belong to the dusty star-forming galaxy population bulk at the peak of cosmic star formation. Several works have demonstrated the effectiveness of submm surveys in selecting strong-lensing events by adopting a flux density threshold of 100 mJy at 500  $\mu\text{m}$ , corresponding to a steep drop in the number counts of dusty star-forming galaxies at submm wavelengths (Blain 1996; Negrello et al. 2010; Lapi et al. 2012), where, thanks to the magnification, they emerge as the bright tail of the population count distribution, thereby minimizing the probability of possible contaminants, such as flat-spectrum radio sources and low-redshift spiral galaxies.

Moreover, in the FIR/submm regime, although the high- $z$  lensed dusty star-forming galaxies are particularly bright, negligible signal comes from the foreground lenses, which are often massive ellipticals at  $z < 1$  that dominate the signal in optical bands. Several surveys that have been conducted with the Herschel Space Observatory over the last decade have led to the discovery of numerous strong-lensing events. The Herschel Multi-tiered Extragalactic Survey (HerMES; Oliver et al. 2012) identified 11 lensed galaxies over 95  $\text{deg}^2$  (Wardlow et al. 2013), while Nayyeri et al. (2016) selected another 77 lensed galaxy candidates in the HerMES Large Mode survey (HeLMS; Oliver et al. 2012) and the Herschel Stripe 82 Survey (Viero et al. 2014). In particular, the Herschel Astrophysical Terahertz Large Area Survey (H-ATLAS; Eales et al. 2010) is the widest-area (600  $\text{deg}^2$ ) extragalactic survey to be undertaken with Herschel, and it has provided a sample of more than 100,000 dusty star-forming galaxies at high redshift. From the H-ATLAS survey, a sample of 80 strongly lensed dusty star-forming galaxy candidates was selected in Negrello et al. (2017), by means of a simple flux density selection ( $S_{500\mu\text{m}} > 100$  mJy). Only 21 of these have been confirmed as being lensed thus far. Recently, another sample of 11 candidates was selected by Ward et al. (2022) from the H-ATLAS third data release, conducted at the South Galactic Pole. The recent work of Shu et al. (2022) has exploited the lensing effects that are generated from galaxy clusters, in order to systematically search for optically dark galaxies. The follow-ups to their sample performed with JCMT/SCUBA ( $\sim 850 \mu\text{m}$ ) and ALMA ( $\sim 870 \mu\text{m}$ ) reached flux limits  $\sim$ three times deeper

than blank fields, highlighting the capabilities of gravitational lensing in detecting even more hidden and dark objects.

In this work, we present lens modeling, source reconstruction, and spectral energy distribution (SED) analyses of HATLASJ113526.3–014605 (hereafter, J1135), also called G12v2.43 or G12H43—an optical/NIR-dark strongly lensed galaxy at  $z = 3.1276$ , from the Negrello et al. (2017) lensed candidate sample, featuring a flux density at 500  $\mu\text{m}$ , amounting to  $204 \pm 8.6$  mJy. The plan of the paper is as follows. In Section 2, we present the target of our analyses and describe the archival ALMA observations and the available ancillary data in other bands. Sections 3 and 4 then describe the lens modeling, source reconstruction, and SED fitting analyses, respectively. Finally, we discuss and summarize our results in Sections 5 and 6. Throughout this work, we adopt the standard flat  $\Lambda$ CDM cosmology (Planck Collaboration et al. 2020), with rounded parameter values: matter density  $\Omega_M = 0.32$ , dark energy density  $\Omega_\Lambda = 0.63$ , baryon density  $\Omega_b = 0.05$ , Hubble constant  $H_0 = 100h$   $\text{km s}^{-1} \text{Mpc}^{-1}$ , with  $h = 0.67$ , and mass variance  $\sigma_8 = 0.81$ , on a scale of  $8 h^{-1}$  Mpc. At the redshift of the source,  $1''$  corresponds to 7.8 kpc.

## 2. The Target

J1135 is part of the sample of 80 (candidate) strongly lensed galaxies (Negrello et al. 2017) that are located in the equatorial GAMA 12th field (R.A. = 11:35:26, decl. =  $-01:46:07$ , J2000). The spectroscopic redshift  $z = 3.1276$  of the background lensed source was obtained from blind CO searches with the Zpectrometer ultrawideband spectrometer on the Green Bank Telescope (GBT; Harris et al. 2012) and confirmed by Northern Extended Millimeter Array (NOEMA) observations (Yang et al. 2017). So far, no redshift measurement is available for the foreground lens. Andreani et al. (2018) presented observations of high-CO transition ( $J = 7\text{--}6$ ) obtained with the Atacama Pathfinder EXperiment (APEX)/SEPIA band 5 receiver for the background object. From a comparison of the CO(7–6) transition with the CO(1–0) and CI(2–1) ones, the authors pointed out the presence of a large excitation status in the ISM of J1135.

Moreover, Vishwas et al. (2018) reported bright [OIII] 88  $\mu\text{m}$  emission for J1135, detected through the z Early Universe Spectrometer on APEX, attributed to ionized hydrogen regions around massive stars. From the SED fitting of the multiband photometry of J1135, the authors predicted J1135 to be a young, gas-rich starburst galaxy.

The object has also been targeted by Submillimeter Array (SMA) high-spatial resolution ( $\sim 0''.8$ ) observations, described in Bussmann et al. (2013), but only marginally resolved. For this reason, its lensed nature has been debated in the works described above.

### 2.1. ALMA Observations

The object is part of the low-resolution ( $\lesssim 2''$ ) observations in band 3 (2017.1.01694.S; PI: Oteo), which were aimed at tracing dense molecular gas through  $J = 4\text{--}3$  transitions of HCN, HCO+, and HNC molecules. J1135 was also included in a project (2019.1.00663.S; PI: Butler) with the main goal of investigating the outflows in high-redshift star-forming galaxies, by tracing the OH+ and CO(9–8) lines.

In the following, we describe the calibration, imaging, and analysis of further data sets with the highest available angular

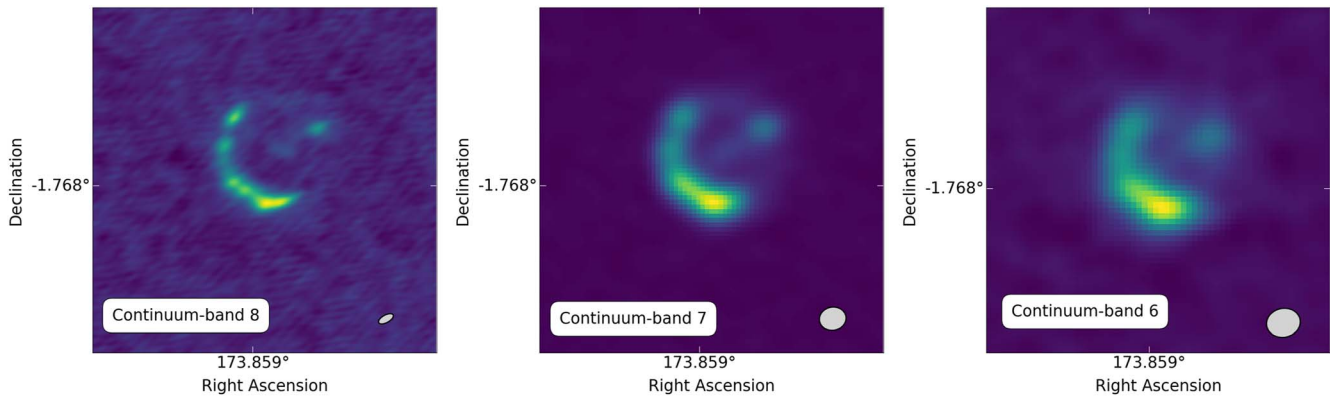


**Figure 1.** ALMA band 8, 7, and 6 continuum emission for J1135. The synthesized beam is displayed in the bottom right corner; the postage stamps are  $3'' \times 3''$ .

**Table 1**  
Overview of the ALMA Observations Used in This Paper

	Cycle 4 B8	Cycle 6 B6	Cycle 6 B7
Project ID	2016.1.01371.S	2018.1.00861.S	2018.1.00861.S
Spectral setup [MHz]	$4 \times 128 \times 15.63$	$4 \times 240 \times 7.81$	$4 \times 240 \times 7.81$
Spectral resolution [ $\text{km s}^{-1}$ ]	10.17	10.48	...
Restored beam axes [ $\text{arcsec}^2$ ]	$0.14 \times 0.07$	$0.29 \times 0.25$	$0.23 \times 0.2$
Continuum sensitivity [ $\text{mJy beam}^{-1}$ ]	0.541	0.043	0.025
Lines	C[II]	CO(8–7)	...

**Note.** The  $\text{H}_2\text{O}$  lines in the Cycle 6 Data are not analyzed in this work.

resolution in the ALMA Science Archive for J1135. These spatially resolved ALMA follow-ups reveal an almost complete Einstein ring, confirming with no doubt the lensed nature of this system.

The object has been the target of an ALMA Cycle 4 high-resolution follow-up in band 8 (2016.1.01371.S; PI: Vishwas), which aimed to resolve the lensed morphology of the source as well as trace the continuum at  $\sim 0.7$  mm and the C[II]  $158 \mu\text{m}$  FIR line. The continuum was observed to exploit four basebands of width 1.98 GHz, centered at 472.284, 470.451, 460.409, and 458.534 GHz, and composed of 128 channels each.

We recalibrated the raw data by using the Common Astronomy Software Applications (CASA; McMullin et al. 2007) package, version 4.7.2, and running the provided calibration scripts. The continuum subtraction was done manually, using the task `uvcontsub`. The imaging was also performed manually, by adopting a Briggs weighting scheme, which assumes a robustness factor of 0.5. The properties of the generated images are reported in Table 1, while the continuum-cleaned images are shown in Figure 1. Figure 2 reports the C[II] spectral line profile and the moment maps corresponding to the integrated brightness, the velocity distribution, and the velocity dispersion.

The second data set that we examine is part of the ALMA Cycle 6 project (2018.1.00861.S; PI: Yang), which was carried out with the goal of tracing  $\text{H}_2\text{O}$  and CO ( $J = 8-7$ ) lines in candidate lensed galaxies at high redshift ( $z \sim 2-4$ ) in bands 6 and 7. Both observations were performed using the same configuration, with a maximum baseline of 1397 m and four spectral windows of 1.875 GHz bandwidth and  $240 \times 7.8$  MHz channels each. In band 6, the  $\text{H}_2\text{O}(J = 2_{0,2}-1_{1,1})$  and CO( $J = 8-7$ ) are targeted with two spectral windows, centered at 239.376 GHz and 223.583 GHz, respectively, while the two

other windows, centered at 235.940 and 221.705 GHz, are dedicated to continuum observations. In Band 7, two spectral windows, centered at 281.766 and 292.621 GHz, target the  $\text{H}_2\text{O}(J = 3_{2,1}-3_{1,2})$  and  $\text{H}_2\text{O}(J = 4_{2,2}-4_{1,3})$  lines, while the continuum is observed in two windows centered at 280.314 and 294.266 GHz.

Calibration is performed by running the available pipeline scripts in CASA version 5.4.0–68. Imaging is performed manually, adopting a Briggs weighting scheme in both bands 6 and 7, with a robustness parameter equal to 0.5. We image the CO(8–7) line by performing an automatic continuum subtraction. Figure 3 shows the CO(8–7) spectral line profile and moment maps.

The main features of the ALMA data analyzed in this work and the properties of the final images are reported in Table 1. Note that the  $\text{H}_2\text{O}$  data cubes included in the Cycle 6 observations will not be analyzed in this paper.

## 2.2. Data Analysis

The flux densities derived for the continuum emission of the lensed source are reported in Table 2. We also include the flux density values measured from the archival image of the Band 3 continuum emission mentioned in Section 2. The flux density uncertainties are computed by including at least a 5% estimation of the flux calibration accuracy (ALMA proposer’s Guide):<sup>8</sup>

$$\delta S_{\text{image}} = \sqrt{N(\sigma_{\text{image}})^2 + (0.05 \times S_{\text{image}})^2}, \quad (1)$$

with  $\sigma_{\text{image}}$  being the rms and  $N$  the number of resolution elements inside the aperture adopted to extract the flux density.

<sup>8</sup> <https://almascience.eso.org/documents-and-tools/cycle6/alma-proposers-guide>

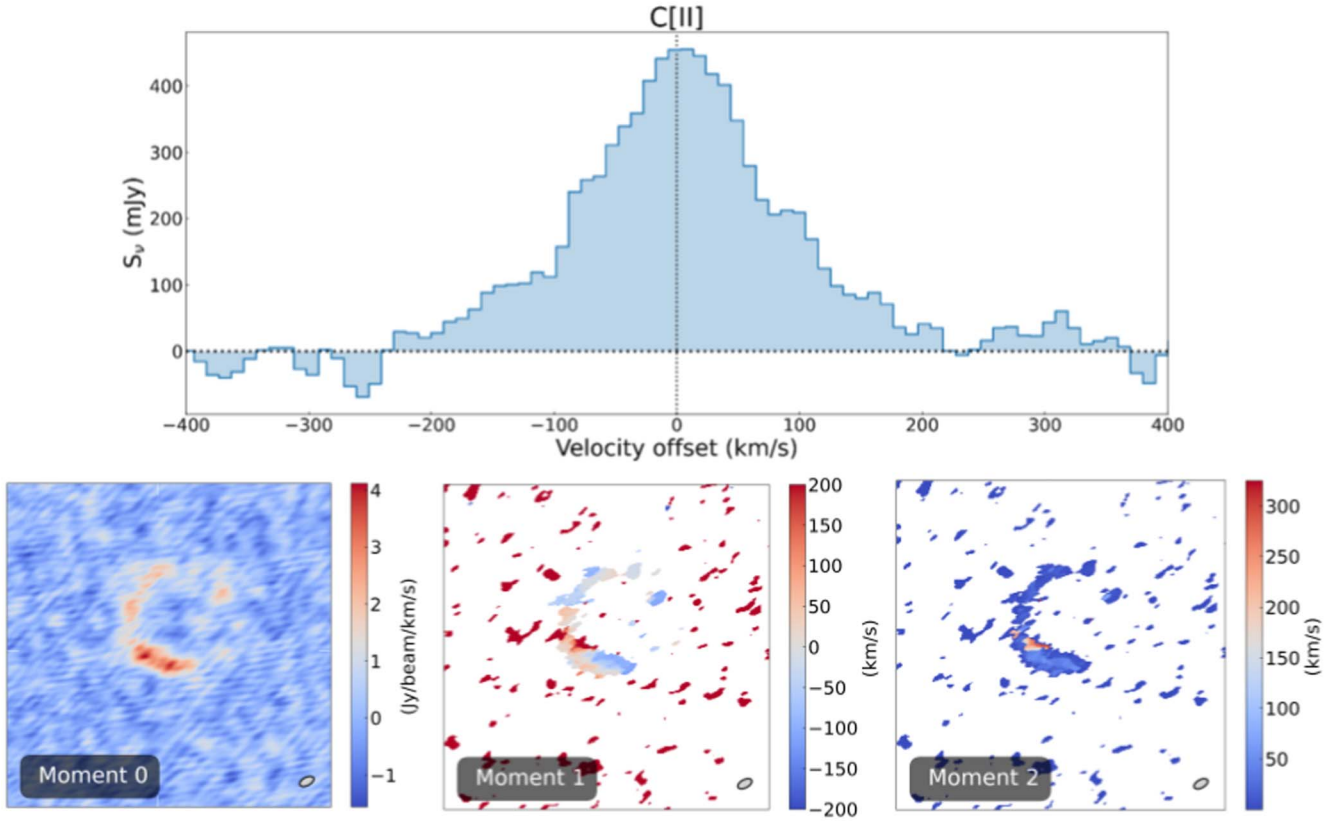


**Figure 2.** Moment maps and the spectral emission of the C II line emission for J1135. From the left: the integrated intensity, line-of-sight velocity, and velocity dispersion. The synthesized beam is displayed in the bottom right corner; the postage stamps are  $3'' \times 3''$ .

By fitting the resolved ALMA spectral lines with a single Gaussian profile, we obtain the FWHM values for both the CO(8–7) and C[II] lines, corresponding to  $215. \pm 4$  and  $181 \pm 5 \text{ km s}^{-1}$ , respectively, in concordance with what is found for the GBT and NOEMA CO and H<sub>2</sub>O lines analyzed in Harris et al. (2012) and Yang et al. (2017). The peaks are detected at  $\nu_{\text{obs}} = 460.504 \pm 0.003 \text{ GHz}$  for C[II] and  $\nu_{\text{obs}} = 223.356 \pm 0.0011 \text{ GHz}$  for CO(8–7), confirming the redshift estimate by Harris et al. (2012) of 3.127, with associated uncertainties of  $\delta z_{\text{C[II]}} = \pm 0.005$  and  $\delta z_{\text{CO(8-7)}} = \pm 0.003$ , respectively. The observed magnified line profiles measured within a region containing the whole source emission are shown in Figures 2 and 3. Following Carilli & Walter (2013), we compute the observed magnified C[II] and CO(8–7) luminosities, expressed in units of  $\text{K km s}^{-1}$ , as:

$$L'_{\text{line}} = 3.25 \times 10^7 \times S_{\text{line}} \Delta v \frac{D_L^2}{(1+z)^3 \nu_{\text{obs}}^2}, \quad (2)$$

where  $S_{\text{line}} \Delta v$  is the measured flux of the line profile (in units of  $\text{Jy km s}^{-1}$ ) and  $D_L$  is the luminosity distance. The luminosities expressed in  $L_{\odot}$  are computed as  $L'_{\text{line}} = 3 \times 10^{-11} \nu_{\text{rest}}^3 L'_{\text{line}}$ . The final values computed for the C[II] and CO(8–7) lines are summarized in Table 3.

### 2.3. Other Bands

J1135 is covered by several surveys, such as the Kilo-Degree Survey (de Jong et al. 2013) and the Hyper Suprime-Cam Subaru Strategic Program in the UV/optical bands (Aihara et al. 2018, 2022), the VISTA Kilo-degree Infrared Galaxy Public Survey (VIKING; Edge et al. 2013) and the UK Infrared

Deep Sky Survey Large Area Survey (Lawrence et al. 2007) in the NIR, and the Wide-field Infrared Survey Explorer (WISE; Wright et al. 2010) in the MIR. PACS and SPIRE FIR observations are reported in the H-ATLAS first and second data release catalogs (Valiante et al. 2016; Maddox et al. 2018). Moreover, the source is also covered by the VLA Faint Images of the Radio Sky at Twenty-Centimeters (Becker et al. 1995) survey in the radio band, where no emission is detected.

High-resolution NIR follow-up observations are available for J1135. The target was observed as part of the Cycle 19 HST/WFC3 snapshot program (PI: Negrello), at a wavelength of  $\lambda = 1.15 \mu\text{m}$  (see Negrello et al. 2014 for further details of the observations), and with the Keck telescope in adaptive optics in the Ks band (Calanog et al. 2014). No successful detection has been found in the Ks image, while a marginal emission ( $\lesssim 3\sigma$ ) is present in the HST image; however, given the insufficient sensitivity and angular resolution, it is not possible to unambiguously confirm whether it is associated with the foreground lens or the background source.

The object has also been detected in MIR observations that are available in the Spitzer/IRAC Data Archive (PI: Cooray; ID: 80156) and are described in Ma et al. (2015), covering IRAC channel 1 and channel 2, at  $3.6 \mu\text{m}$  and  $4.8 \mu\text{m}$ , respectively.

In addition, we find EVLA radio data in the NRAO Archive, particularly follow-ups in the C band centered at  $\sim 6 \text{ GHz}$  (project code: 16A-240; PI: Smith). The data are processed by running the calibration scripts, while cleaning is performed manually with CASA, adopting an interactive mask. The final image reaches a mean rms of  $\sim 0.013 \text{ mJy beam}^{-1}$  and a restored beam ellipse of  $1''.13 \times 0''.84$  (see Figure 4).

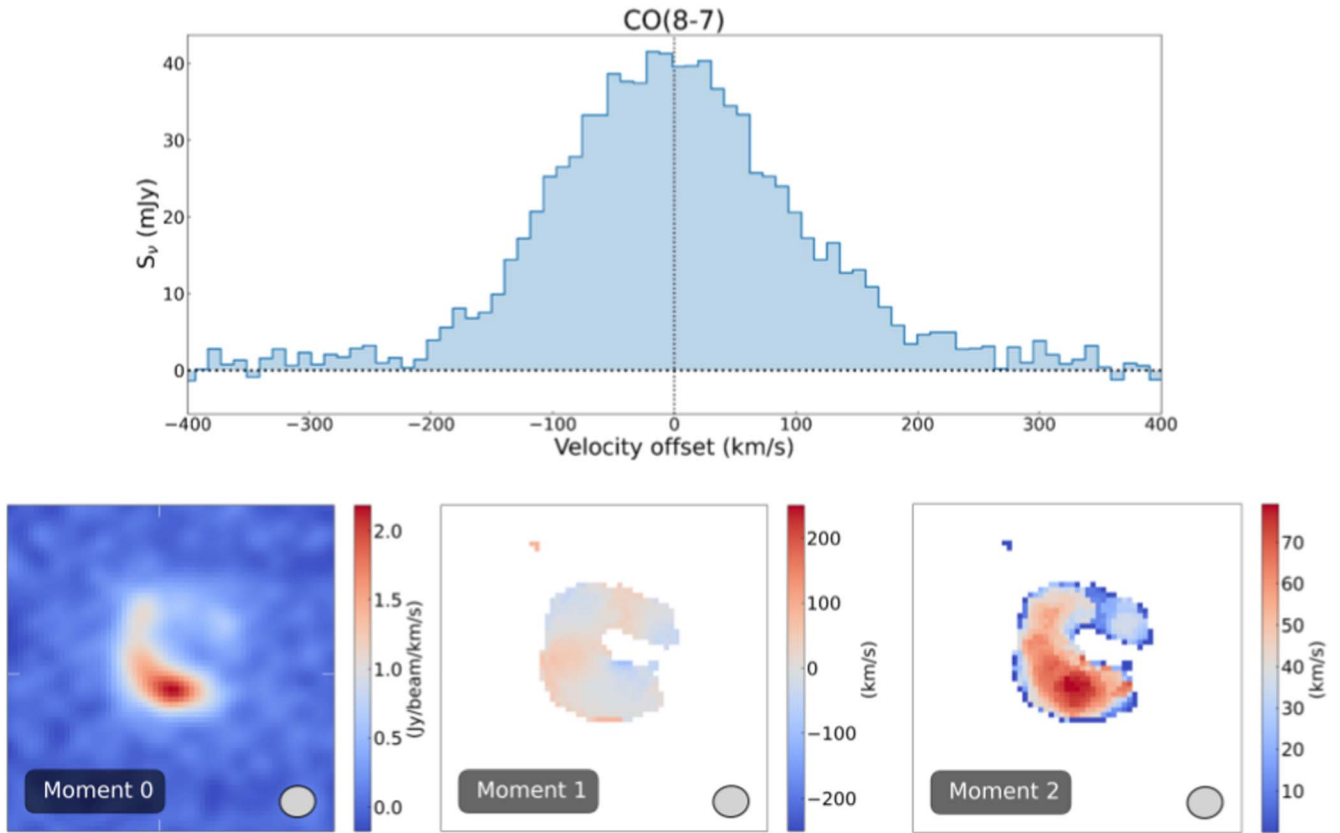


Figure 3. The same as Figure 2, but for the CO(8–7) line emission for J1135.

The multiband (optical-to-MIR) image cutouts of J1135 are reported in Figure 5. A faint emission at  $\sim 4\sigma$  emerges, starting in the VIKING H band and being detected in both IRAC channels, with a signal-to-noise ratio (S/N)  $\gtrsim 6$ , but the angular resolution is not sufficient to resolve any lensing features (e.g., arcs) in the NIR/MIR regime. The flux densities are estimated by performing aperture photometry, with aperture diameters of  $2''$  for NIR VIKING images and  $6''$  for Spitzer/IRAC images. Table 2 summarizes the photometry for J1135; we report the upper limits for nondetections (i.e., emission with  $S/N \lesssim 3$ ).

### 3. Lens Modeling and Source Reconstruction

In order to reconstruct the intrinsic background source morphology, we perform lens modeling analysis with the open source Python 3.6+ code `PyAutoLens` (Nightingale et al. 2018, 2021), which implements the regularized semilinear inversion (SLI) method described in Warren & Dye (2003), together with the adaptive source plane (SP) pixelization scheme described in Nightingale & Dye (2015), and adapted to interferometric data as done in Massardi et al. (2018), Dye et al. (2018), Enia et al. (2018), Dye et al. (2022), Maresca et al. (2022), and as detailed in Appendix.

#### 3.1. Lens Model

In reconstructing the source’s light profile, we first need to assume a density profile for the mass of the foreground object. The lens is modeled as a singular isothermal ellipsoid (Kormann et al. 1994), i.e., an elliptical power-law density distribution that follows  $\rho \propto r^{-\gamma}$ , with  $r$  being the elliptical

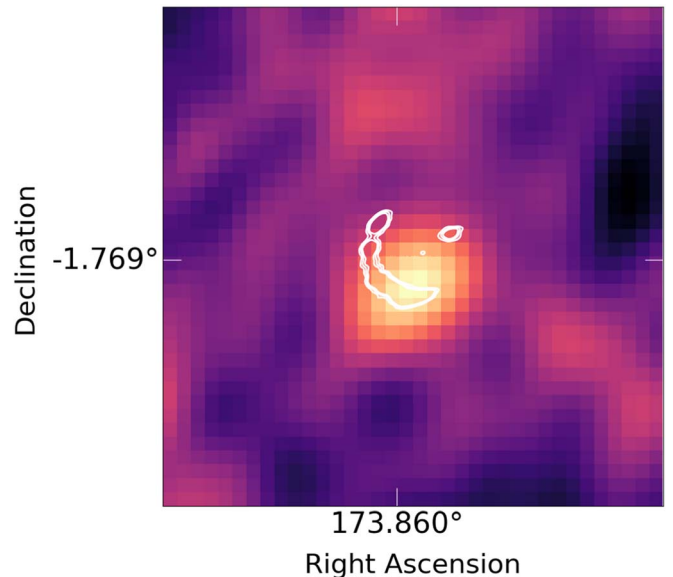
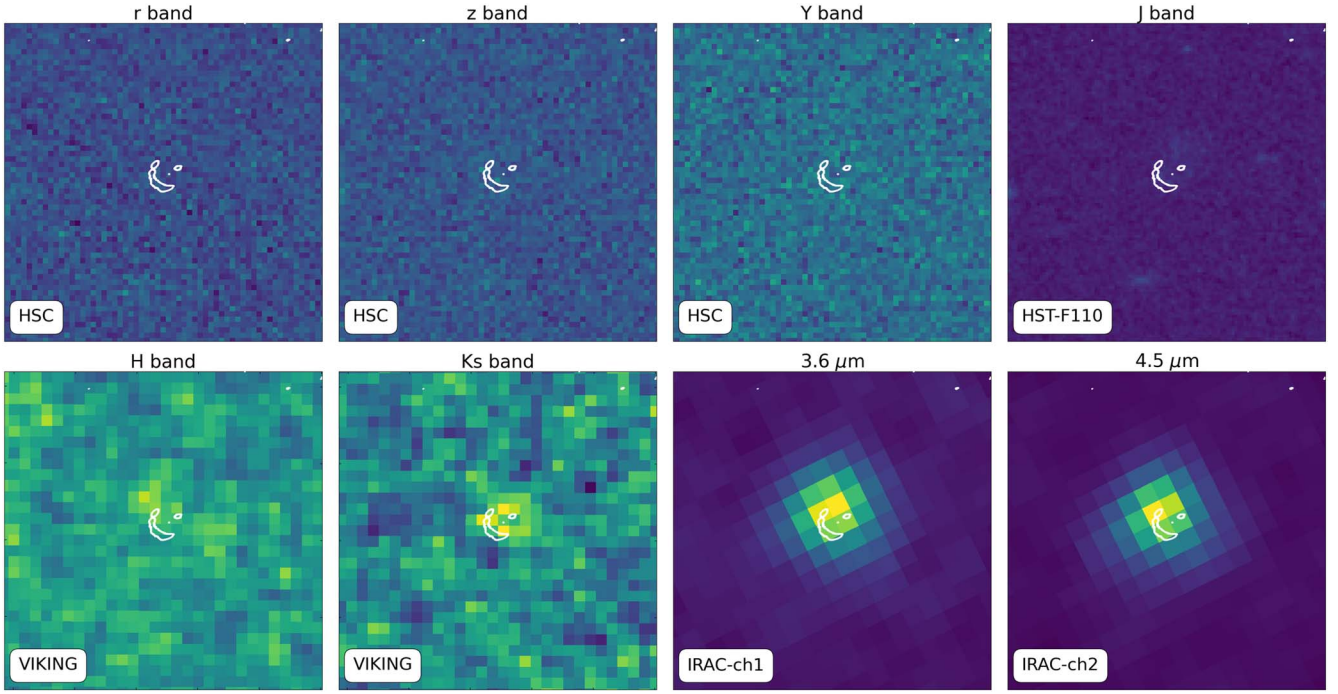


Figure 4. Image of the EVLA detection at 6 cm for J1135. The white contours represent the ALMA continuum emission in band 8 at  $9\sigma$ ,  $7\sigma$ , and  $5\sigma$ .

radius, and with a fixed slope value  $\gamma=2$ . The profile is described by five parameters: the Einstein radius  $\theta_E$ , the lens centroid positions  $x_c$ ,  $y_c$ , and the first and the second ellipticity components of the elliptical coordinate system ( $e_x$ ,  $e_y$ ). The latter originate from two quantities: the positional angle ( $\phi$ ), defined counterclockwise from the positive  $x$ -axis, and the factor  $f=(1-q)/(1+q)$ , where  $q$  is the ratio between the



**Figure 5.** Cutouts of the optical-to-MIR images for J1135 centered on the Herschel position. The contours display the ALMA band 8 continuum emission at  $9\sigma$ ,  $7\sigma$ , and  $5\sigma$ . The postage stamps are  $10'' \times 10''$ .

semimajor and semiminor axis. The final expressions for the elliptical components are:

$$\begin{aligned} e_y &= f \times \sin(2\phi), \\ e_x &= f \times \cos(2\phi). \end{aligned} \quad (3)$$

From several tests, we have verified that the shear component does not improve the model, but rather worsens the fit results, and for this reason it has been omitted.

PyAutoLens performs lens fitting through the nested sampling algorithm *Dynesty* (Speagle 2020), which samples the parameter space and computes the posterior probability distributions for the parameters of a given lens model.

Our searching chain consists of two steps. (1) We search for the best-fit lens model through nonlinear parametric fitting. We assume the source light to be described by a Sérsic profile and simultaneously fit the ALMA data in all three bands (including spectral lines). (2) Keeping the best-fit lens model parameters obtained in the first step fixed, we then perform the inversion. The fit is performed on a number of pixels delimited by a circular mask, where the radius changes according to the resolution of the cleaned ALMA image, in order to obtain a satisfactory fit that is not excessive in terms of the computational cost.

### 3.2. Results

The best-fit lens model is described by the following parameters:  $\theta_{\text{Ein}}^{\text{mass}} = 0.4241_{-0.0005}^{+0.0005}$ ,  $y^{\text{mass}} = -0.2329_{-0.0005}^{+0.0005}$ ,  $x^{\text{mass}} = 0.1494_{-0.0009}^{+0.0011}$ ,  $q = 0.637_{-0.001}^{+0.001}$ , and  $\phi = -35.31_{-0.04}^{+0.04}$ . The best-fit parameters and their uncertainties in the outputs from the parametric nonlinear search and inversion procedure are reported in Table 4. This key information allows us to retrieve the intrinsic properties of the lensed background object, which will be discussed in detail in Section 5. The resulting

reconstructed source contains only pixels that have been excluded from the masked lensed image area. The magnification factors are computed as  $\mu = A_{\text{IP},5\sigma}/A_{\text{SP},5\sigma}$ , where  $A_{\text{IP},5\sigma}$  and  $A_{\text{SP},5\sigma}$  are the areas enclosing significant (i.e.,  $>5\sigma$ ) pixels in the reconstructed image plane (IP) and reconstructed SP, respectively. The noise is estimated as the rms in the reconstructed source map. From the area enclosing all the pixels with  $S/Ns \gtrsim 3$  and  $\gtrsim 5$  in the reconstructed SP, the effective radius can be computed as  $r_{\text{eff}} = (A_{\text{SP}}/\pi)^{0.5}$ . In order to determine the uncertainties of these parameters, we exploit the set of samples provided by the nonlinear search that was performed during the inversion. Each sample corresponds to a set of inversion parameters (i.e., the regularization coefficient and the pixelization shape) that were evaluated and accepted by the nonlinear search. The uncertainties are then retrieved as the 16th and 84th quantiles of the parameter distribution drawn from  $\sim 200$  accepted samples.

It is crucial to point out that the robustness of these quantities strongly depends on the noise covariance that, in the case of interferometric source reconstruction, is difficult to quantify (Rizzo et al. 2021; Stacey et al. 2021). In order to understand how much the estimation of the noise impacts on our results, we compare the effective radii inferred from the source reconstruction with the values that we report for the best-fit effective radii of the Sérsic profile ( $R_{\text{eff,par}}$ ) used in the nonlinear parametric fit described in Section 3.1. The values are shown in Table 4. We find that the effective radii inferred from the two different methods are broadly consistent with one another. The only exception is for Band 7, where  $R_{\text{eff,par}}$  is higher with respect to the values computed from the source reconstruction, likely due to a higher noise level. Therefore, the parameter uncertainties from the inversion are likely to be underestimated. Figures 6 and 7 show the original lens plane image, the model image, the normalized residual map, and the

**Table 2**  
Photometric Data for J1135

Wavelength ( $\mu\text{m}$ )	Flux Density	Instrument
0.47	$\lesssim 0.09 \times 10^{-3}$	HSC/g
0.61	$\lesssim 0.17 \times 10^{-3}$	HSC/r
0.77	$\lesssim 0.26 \times 10^{-3}$	HSC/i
0.89	$\lesssim 0.41 \times 10^{-3}$	HSC/z
0.97	$\lesssim 0.43 \times 10^{-3}$	HSC/y
1.15	$\lesssim 0.91 \times 10^{-3}$	HST/WFC3
1.64	$(6.9 \pm 1.2) \times 10^{-3}$	VIKING/H
2.15	$(7.8 \pm 1.2) \times 10^{-3}$	VIKING/Ks
3.55	$(37.1 \pm 6.2) \times 10^{-3}$	Spitzer/IRAC1
4.49	$(58.2 \pm 7.5) \times 10^{-3}$	Spitzer/IRAC2
11.6	$\lesssim 0.45$	WISE/W3 <sup>a</sup>
22.1	$\lesssim 3.83$	WISE/W4 <sup>a</sup>
100	$\lesssim 136.3$	Herschel/PACS <sup>b</sup>
160	$151.5 \pm 50.3$	Herschel/PACS <sup>b,c</sup>
250	$278.8 \pm 7.4$	Herschel/SPIRE <sup>b,c</sup>
350	$282.9 \pm 8.2$	Herschel/SPIRE <sup>b,c</sup>
500	$204.0 \pm 8.6$	Herschel/SPIRE <sup>b,c</sup>
640	$163.7 \pm 8.4$	ALMBA/B8
850	$118.8 \pm 8.5$	SCUBA-2 <sup>d</sup>
880	$48.6 \pm 2.3$	SMA <sup>e</sup>
1043	$29.4 \pm 1.5$	ALMA/B7
1300	$16.2 \pm 0.8$	ALMA/B6
3450	$0.71 \pm 0.04$	ALMA/B3
48100	$0.09 \pm 0.01$	EVLA/BC

**Notes.** We show references for the flux densities (in mJy) taken from the catalogs described in Section 2.3, while the remaining values are extracted through aperture photometry. The upper limits are reported at the  $3\sigma$  level.

<sup>a</sup> From the WISE All-sky Data Release (Wright et al. 2010).

<sup>b</sup> From the H-ATLAS Data Release 1 catalog described in Valiante et al. (2016).

<sup>c</sup> From the H-ATLAS Data Release 2 catalog described in Maddox et al. (2018).

<sup>d</sup> From the Herschel bright sources sample (Bakx et al. 2018).

<sup>e</sup> From the SMA observations described in Bussmann et al. (2013).

**Table 3**  
Properties of the C[II] and CO(8–7) Lines

Line	$\mu\Delta v S_{\text{line}}$ (Jy km s <sup>-1</sup> )	$\mu L$ ( $10^9 L_{\odot}$ )	$\mu L'$ ( $10^{11} \text{K km s}^{-1} \text{pc}^2$ )
C[II]	$82.5 \pm 2.1$	$27.7 \pm 0.7$	$1.35 \pm 0.03$
CO(8–7)	$9.4 \pm 0.1$	$1.54 \pm 0.03$	$0.65 \pm 0.01$

**Note.** From the left: the measured flux from a single Gaussian profile fit, the line luminosity expressed in  $L_{\odot}$ , and the line luminosity expressed in  $\text{K km s}^{-1} \text{pc}^2$ .

reconstructed source for the three ALMA continuum bands and the CO(8–7) and C[II] emission lines, respectively. The differences in the retrieved physical scale values reflect the heterogeneity of the data adopted in this work—the product of different array configurations and angular resolutions. The central feature that emerges in the normalized residuals of the continuum in bands 8, 7, and 6 could originate from the faint foreground lens, the nature of which is discussed in detail in the following section. Our attempt to remove the emission by light profile subtraction was unsuccessful, mainly because of its extreme compact size and faintness compared to the

**Table 4**  
Output Properties of the Lens Modeling and Source Reconstruction Analysis

	$\mu_{\text{rec}}$	$\theta_{\text{rec}}$ (arcsec)	$R_{\text{eff},3\sigma}$ (pc)	$R_{\text{eff},5\sigma}$ (pc)	$R_{\text{eff,par}}$ (pc)
Band 8	$12.80^{+0.32}_{-0.18}$	0.03	$541^{+18}_{-10}$	$392^{+5}_{-13}$	$571^{+160}_{-142}$
Band 7	$8.34^{+0.2}_{-0.05}$	0.07	$518^{+35}_{-70}$	$314^{+64}_{-24}$	$995^{+38}_{-34}$
Band 6	$6.51^{+1.48}_{-1.56}$	0.1	$1146^{+149}_{-158}$	$770^{+157}_{-183}$	$789^{+75}_{-65}$
C[II]	$6.01^{+0.44}_{-0.38}$	0.04	$596^{+43}_{-42}$	$525^{+40}_{-50}$	$764^{+110}_{-50}$
CO(8–7)	$6.22^{+0.79}_{-0.87}$	0.1	$1200^{+106}_{-89}$	$970^{+84}_{-105}$	$936^{+248}_{-270}$

**Note.** From the left: the magnification factor, the demagnified angular resolution, and the effective radius for  $3\sigma$  and  $5\sigma$  emission. The last column reports the best-fit value for the effective radius of the Sérsic profile adopted in the first step of our analysis.

background lensed source. However, the presence of the lens in the continuum bands does not have a considerable impact on the lens model in bands 8 and 7, where we estimate its contribution to be no higher than  $\sim 4\%$  with respect to the lensed source flux density (i.e., computed by including only the light originating by the arcs in the lens plane). One caveat concerns the band 6 continuum, where the contribution of the central emission is estimated to be up to  $\sim 28\%$  of the lensed source flux density, and where the lens modeling results are more difficult to interpret. In this case, the uncertainties have an impact on the estimates of the magnification factors and effective radii, and are included in the errors of these quantities. Since the band 6 continuum is only used in the SED fitting (see Section 4), and given that it is not part of the general discussion, its overall impact on our analysis is negligible. We have decided to keep the lens modeling and the estimated quantities in this paper, since they could be informative for future works regarding J1135.

Moreover, we reconstruct the velocity map for the CO(8–7) line by dividing and modeling the emission in three different velocity bins. As there is no significant difference in the reconstructed emission in the bins, we cannot claim any indications of rotation or outflow (see Figure 8). This is also noticeable in the first moment maps shown in Figure 3, where no strong velocity gradients are visible along the widths of the arcs. The velocity dispersion peak is co-spatial with the integrated brightness peak, located in the southern region of the arc, and corresponding to the northern clump in the reconstructed velocity map. Our attempt to reconstruct the C[II] velocity field was unsuccessful, because of the poor S/N of the individual velocity bins, even though a modest velocity gradient is visible in Figure 2, peaking at the same position as the velocity dispersion.

### 3.3. The Lens

One peculiar aspect of the J1135 gravitational lensed system is the faintness of the foreground object. Indeed, no redshift estimate is available for the lens galaxy, and no clear detection is measured from the photometric images, likely due to insufficient sensitivity and/or angular resolution. A faint central emission is detected in the residuals of the lens modeling, and visible in Figure 6, but it is not clear whether it should be unambiguously associated with the lens or with some spurious emission related to the noise. As shown in analogous studies, and as revealed by HST/NIR high-resolution images (e.g., Negrello et al. 2014), the foreground object usually

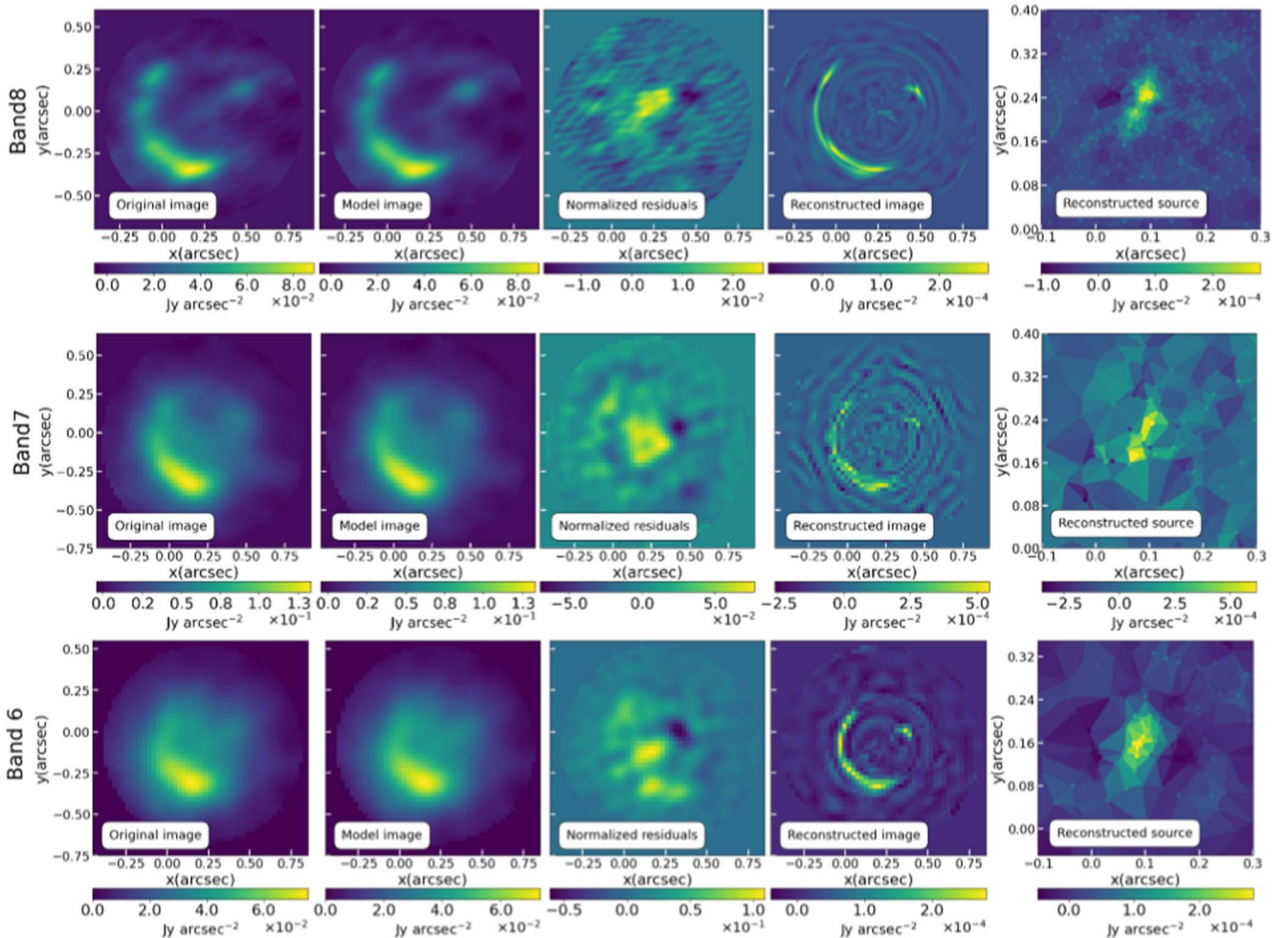


**Figure 6.** The results of the lens modeling and source reconstruction procedure for the continuum data. From the first column to the right: the original ALMA image, the best-fit lensed model image, the residuals, the reconstructed IP, and the reconstructed SP. The residuals are computed as (data model)/noise maps. Please note that the surface brightness values of the former are demagnified. The color bar indicates the surface brightness in units of  $\text{Jy arcsec}^{-2}$ . From the first row down: the continuum emission in bands 8, 7, and 6.

dominates the emission in these bands, with a progressively higher contribution coming from the background source at higher wavelengths. For this reason, in order to achieve reliable results from the SED fitting procedure, it is essential to fit and subtract the light profile of the foreground galaxy. In this case, however, only a marginal emission ( $\lesssim 3\sigma$ ) comes from the HST WFC3/F110 data, and it is not possible to establish a priori whether it originates from the lens or from the lensed object. We therefore explore the assumption of the lens as a massive elliptical, and attribute its faintness to its relatively high redshift (e.g.,  $z \gtrsim 1.5$ ). We model the SED of the foreground object according to this assumption, and we constrain its luminosity by means of the Einstein (total) mass resulting from the lens modeling ( $M_E \sim 1.15 \times 10^{11} M_\odot$ ). Specifically, we adopt the template for an elliptical galaxy with a 2 Gyr age from the SWIRE library (Polletta et al. 2007). The resulting SED of this template, overlapped with the photometry reported in Table 2, is shown in Figure 9. We find the contribution from the lens to be negligible for the flux densities from the  $H$  and  $K_s$  VIKING bands up to higher wavelengths, so no lens subtraction is needed. The situation is less clear for the marginal HST WFC3/F110 detection, and, for this reason, we consider this value as an upper limit.

#### 4. SED Fitting

By correcting the available photometric information for the magnification factors, we can retrieve the intrinsic physical properties of J1135. To achieve this goal, we perform SED fitting with the Code Investigating GALaxy Emission (CIGALE; Boquien et al. 2019). CIGALE is a Python SED-fitting code that is able to reproduce broadband UV-to-radio photometric data according to the energy balance (i.e., the energy coming from the stellar UV–NIR emission is the same as the one re-emitted by the dust in the MIR and FIR regime). The main physical properties are estimated by comparing the observed galaxy SED with the modeled one, by means of a  $\chi^2$  test and Bayesian statistics. We exploit the available broadband photometry described in Section 2.3 and the ALMA continuum emission, including a  $3\sigma$  upper limit for nondetections. For ALMA bands 8, 7, and 6, we correct the flux density values for the respective magnification factors reported in Table 4, while we adopt an average value of  $\sim 9.2$  for low-resolution photometric data. As described in Section 3.3, we adopt the assumption that the observed photometry belongs only to the lensed source. In the following, we describe the modules adopted for the SED-fitting procedure.



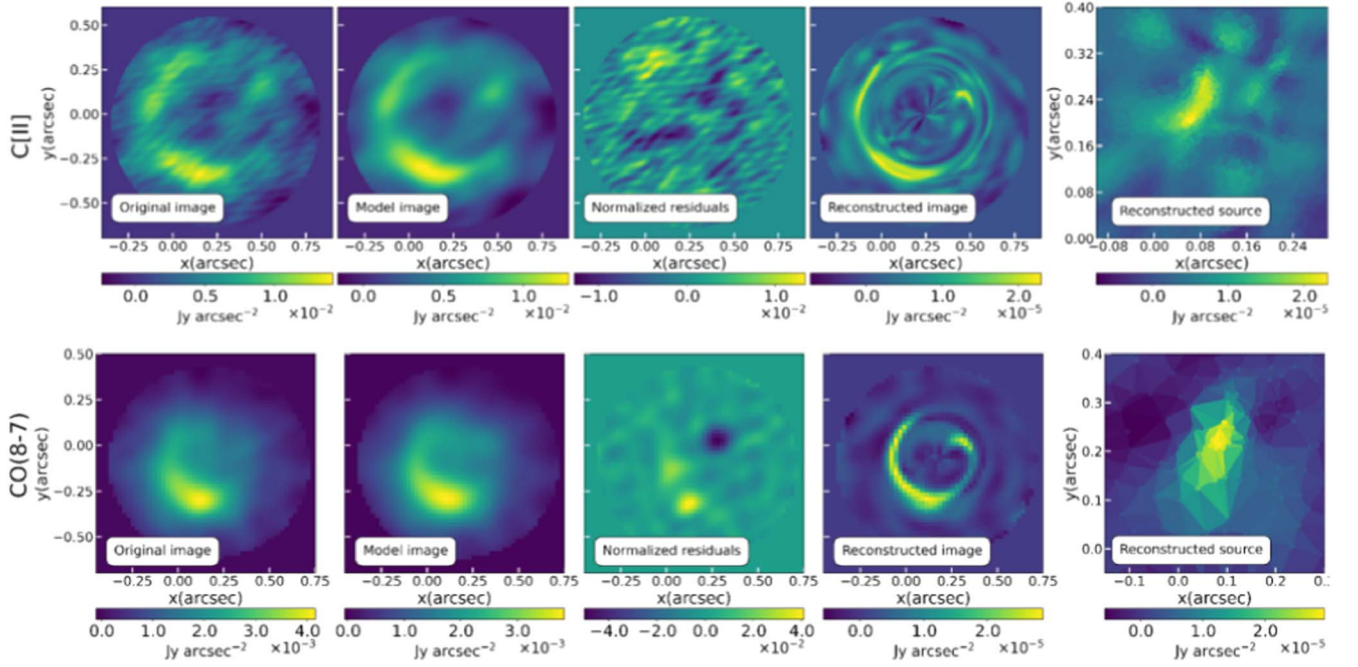


**Figure 7.** The same inputs and outputs as in Figure 6 for the C[II] and CO(8–7) line data, represented in the first and second rows, respectively.

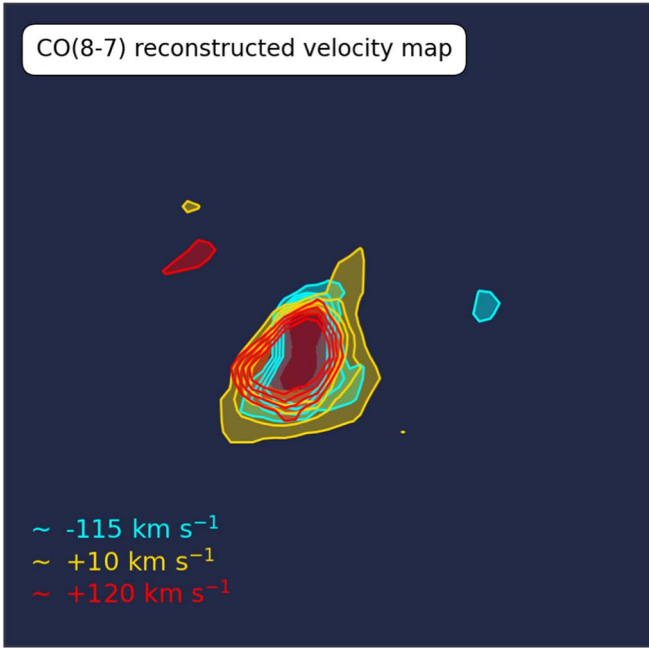


**Figure 8.** Reconstructed velocity map for the CO(8–7) line emission. The contours represent the reconstructed surface brightnesses for three different velocity bins.

The stellar emission is computed following the Bruzual & Charlot (2003) population synthesis models, which are associated with a Chabrier (2003) initial mass function and metallicity values of  $Z=0.004, 0.008, 0.02,$  and  $0.05$ . We assume a delayed star formation history, which predicts a nearly linear increase of the SFR:

$$\text{SFR}(t) \propto \frac{t}{\tau^2} \times \exp\left(-\frac{t}{\tau}\right) \quad \text{for } 0 \leq t \leq t_0, \quad (4)$$

where  $t_0$  is the age of the onset of star formation and  $\tau$  is the time at which the SFR peaks.

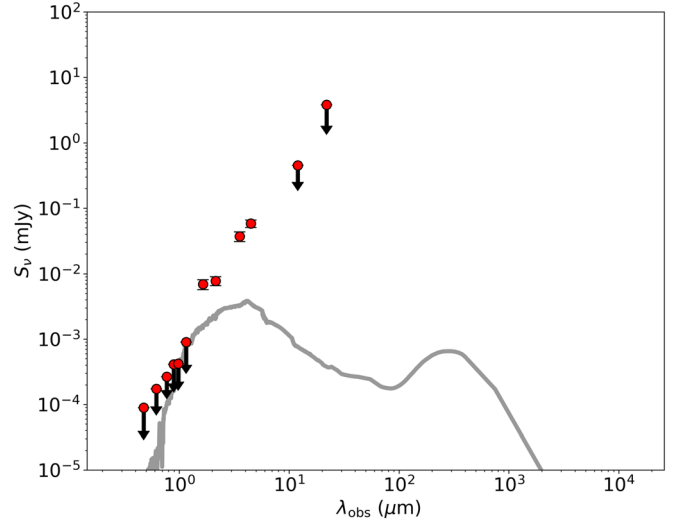


**Figure 9.** SED template of a passive elliptical galaxy at redshift  $z \sim 1.5$  compared with the photometry of J1135. The flux densities reported in Table 2, from HSC/g to WISE-4 ( $22\mu\text{m}$ ), are represented as the red points. The upper limits at  $3\sigma$  are shown as arrows.

In order to model the effect of the dust attenuation on far-UV–optical light, we adopt the modified Charlot & Fall (2000) prescriptions, where the attenuation is age-dependent and described by two different power laws, one for the ISM and one for the birth clouds (BC). The attenuation slopes are assumed to be  $-0.7$  and the V-band attenuation is computed as:

$$\kappa = \frac{A_V^{\text{ISM}}}{A_V^{\text{ISM}} + A_V^{\text{BC}}}. \quad (5)$$

In our analysis, we assume  $A_V^{\text{ISM}}$ , spanning from 0.3 to 5.0, and a  $\kappa$  spanning from 0.3 to 0.6.

Following Draine & Li (2007), the dust emission is modeled as two separated components: a diffuse component, which is illuminated with a single radiation field ( $U_{\text{min}}$ ) originating from

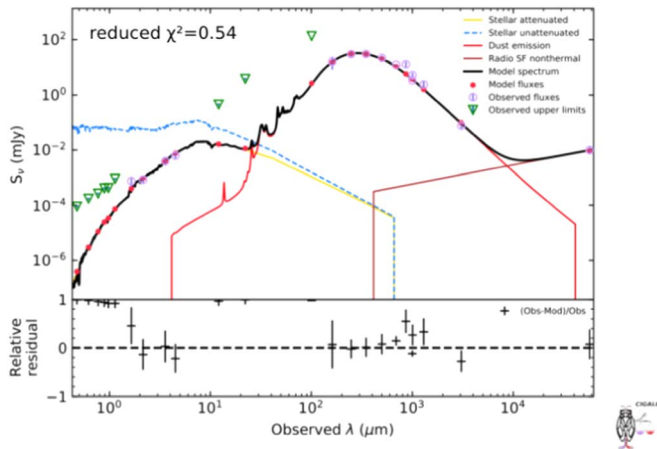


**Figure 10.** The best-fit UV-to-radio observed-frame SED of J1135. The green arrows show the  $3\sigma$  upper limits, while the purple circles show the observed flux densities and errors. The black line is the best-fitting MBB spectrum.

a general stellar population; and a second component that is closely associated with the regions in which the star formation occurs, heated by a variable radiation field described with a power-law profile and defined between two values,  $U_{\min}$  and  $U_{\max}$ . In particular, we use the most recent and refined version of this model, which also accounts for dust mass renormalization (Draine et al. 2014).

The best-fit model is presented in Figure 10, and the resulting best physical properties are summarized in Table 5.

## 5. Discussion

Taking advantage of the SED fitting results and the reconstructed morphologies, we are able to investigate the ISM conditions of J1135 and its evolutionary state.

### 5.1. Dust Properties

Table 5 reports the best-fit dust mass estimated by CIGALE. The main advantage of choosing the Draine et al. (2014) multiparameter library is due to its physical motivation, as the dust is indeed described as a mixture of carbonaceous and amorphous silicate grains. This results in a more robust estimate of the dust mass ( $M_{\text{dust}}$ ) with respect to a single-temperature modified blackbody (MBB) fit, which tends to underestimate  $M_{\text{dust}}$  by a factor of  $\sim 2$  (Magdis et al. 2012; Berta et al. 2016), resulting in a wrong gas mass derivation. Another issue has to do with the dust temperature estimation of high-redshift star-forming galaxies. Different results in the literature (e.g., Riechers et al. 2013; Spilker et al. 2016; Scoville et al. 2017; Simpson et al. 2017; Jin et al. 2019; Cortzen et al. 2020; Jin et al. 2022) suggest that the widely adopted optically thin MBB approximation may not be sufficient for inferring the highest dust temperatures for dusty and optically thick galaxies. For example, Jin et al. (2019) and Jin et al. (2022) reported the presence of a population of compact high-redshift ( $z \sim 4$ ) starbursts, selected in the FIR with Herschel and detected with ALMA and NOEMA, showing abnormally cold dust temperatures. This behavior can either be associated with low star formation efficiency (SFE), accompanied by the rapid enrichment of metals, or with a dust continuum in an optically thick FIR regime (Cortzen et al. 2020).

**Table 5**  
Best-fit Output Parameters from CIGALE—from the First Row: Dust Luminosity, Dust Mass, SFR, Stellar Mass, and the IRRC Parameter

SED-fitting Results	
$\log L_{\text{dust}} (L_{\odot})$	$13.03 \pm 0.06$
$\log M_{\text{dust}} (M_{\odot})$	$9.06 \pm 0.04$
$\log \text{SFR} (M_{\odot} \text{ yr}^{-1})$	$2.97 \pm 0.08$
$\log M_{\star} (M_{\odot})$	$\lesssim 11.75$
$q_{\text{IR}}$	$2.84 \pm 0.09$

Following Cortzen et al. (2020), we compute the dust temperatures using three different approaches: from the CIGALE results, we adopt the physically motivated Draine et al. (2014) model, we assume an optically thin MBB, and we assume an optically thick MBB. The Draine & Li (2007) and Draine et al. (2014) model assumes an optically thin dust emission and does not provide a luminosity weighted temperature. However, following Draine (2011), we retrieve the dust temperature as  $T_{\text{dust,DL14}} = 20U_{\min}^{1/6}$  K, where  $U_{\min}$  is the value of the minimum intensity of the radiation field, as inferred from CIGALE. From the best-fit value of  $U_{\min} = 44.3 \pm 10.6$ , we obtain a dust temperature of  $T_{\text{dust,DL14}} = 37.7 \pm 1.5$  K.

By exploiting the available FIR-to-submm photometry, we then fit a single-temperature MBB under the optically thin approximation, described as

$$S_{\nu} \propto \frac{\nu^{3+\beta}}{e^{(h\nu/kT_{d,\text{thin}})} - 1}, \quad (6)$$

where  $k$  is the Boltzmann constant and  $\beta$  is the dust emissivity index, which is here assumed to be  $\beta = 2$ . Similarly, for the optically thick regime, we fit the single-temperature MBB defined as

$$S_{\nu} \propto (1 - e^{-\tau_{\nu}}) \frac{\nu^3}{e^{(h\nu/kT_{d,\text{thick}})} - 1}, \quad (7)$$

with  $\tau_{\nu} = (\nu/\nu_0)^{\beta}$  and  $\nu_0$  being the rest-frame frequency corresponding to a dust opacity equal to unity.

The best-fit results for both the optically thin and optically thick approximations are represented in Figure 11. The resulting dust temperatures are  $T_{\text{dust,thin}} = 38.6 \pm 1.1$  K and  $T_{\text{dust,thick}} = 64.8 \pm 2.8$  K, respectively, where the former is consistent with  $T_{\text{dust,DL14}}$ .

From our analysis, we derive a significant discrepancy between  $T_{\text{dust,thin}}$  and  $T_{\text{dust,thick}}$ , which is apparently in agreement with what has been observed for similar objects in the literature. In particular, the recent work of Jin et al. (2022) has presented useful diagnostics that can be adopted to identify whether an optically thick model is more appropriate for describing dust emission (e.g., the SFE and the position relative to the IR luminosity surface density diagram). By taking advantage of these indicators, we investigate the nature of the dust continuum emission of J1135. The star formation surface density that we retrieve in Section 5.3 is well above the threshold suggested by the authors for the optically thick regime (i.e.,  $\Sigma_{\text{SFR}} \gtrsim 20 M_{\odot} \text{ yr}^{-1} \text{ kpc}^{-2}$ ). Moreover, the dust temperature that is inferred from the optically thin approximation implies  $\Sigma_{\text{IR}} \gtrsim 1.5 \times 10^5 T_{\text{dust,thin}}^{4.21}$ , which is inconsistent with the Stefan–Boltzmann law, representing the upper boundary for an object to emit as a blackbody. In Figure 12, we show the dust temperature against the intrinsic IR

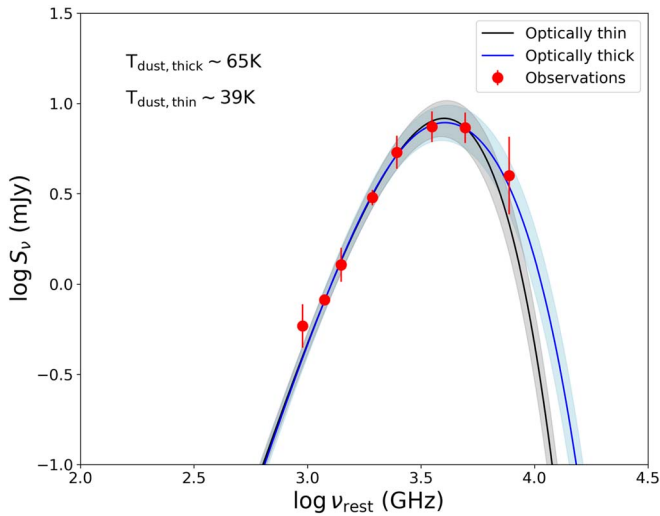


**Figure 11.** The best-fit FIR-to submm rest-frame SED of J1135. The red points are the observed flux densities and errors, while the black and blue lines are the best-fitting MBB spectra in the optically thin and thick regimes, respectively. The gray shaded area represents the 68% confidence interval for the best-fit model.

luminosity ( $\propto$ SFR), color coded in relation to the effective radius for J1135. We compare our source to other samples of DSFGs, according to its position with respect to the modified Stefan–Boltzmann law inferred by Yan & Ma (2016), for different effective radii. As expected, temperatures of the order of  $T_{\text{dust,thin}}$  and  $T_{\text{dust,DL14}}$  would imply effective radii  $\gtrsim 1.5$  kpc at the inferred  $L_{\text{dust}}$  (hereafter,  $L_{\text{IR}}$ ), which are well above what we measure from the reconstructed dust continuum morphology. In this plot, we therefore assume the case  $T_d = T_{\text{dust,thick}}$ , obtaining a more consistent result. This is indeed in concordance with what Jin et al (2022) predicted for apparently cold starbursts, disfavoring the low-efficiency star formation mechanism accompanied by fast metal enrichment.

We then compare J1135 with other samples of DSFGs: we include the sample of apparently cold FIR-selected starbursts from Jin et al (2022) in the redshift range  $3 \lesssim z \lesssim 6$ , the sample of FIR-to-submm-selected lensed quasars ( $1.5 \lesssim z \lesssim 2.5$ ) from Stacey et al. (2021), and, finally, the sample of lensed DSFGs selected by Herschel (Nayyeri et al. 2016; Negrello et al. 2017), and analyzed in works by Nayyeri et al. (2016) and Dye et al. (2018), distributed over the range  $1 \lesssim z \lesssim 4$  (the values are reported in Table A.1. of Stacey et al. (2021)). J1135 shows smaller sizes compared to other lensed DSFGs at similar luminosities ( $L_{\text{IR}} \gtrsim 10^{13} L_{\odot}$ ) and temperatures that are comparable with some of the warmer lensed quasars.

### 5.2. Stellar and Gas Masses

The available data allow us to estimate the gas content by adopting several empirical calibrators. First, we directly estimate the gas mass from C[II]: following Zanella et al. (2018), we assume  $\alpha_{\text{C[II]}} \equiv M_{\text{gas}}/L_{\text{C[II]}} = 22 M_{\odot}/L_{\odot}$ , which is calibrated from starburst galaxies spanning a redshift range  $z \sim 2$ –6. Second, in order to estimate the molecular gas content ( $M_{\text{H}_2}$ ), we derive the  $L'_{\text{CO}(1-0)}$  from the demagnified  $L'_{\text{CO}(8-7)}$  luminosity. We then follow Fujimoto et al. (2022), by adopting a conversion factor of  $L'_{\text{CO}(1-0)} = 1.5L'_{\text{CO}(7-6)}$ , as estimated for high-redshift starburst galaxies in the literature (e.g., Riechers et al. 2013). This conversion factor is referred to a different transition, corresponding to the higher luminosity

values of the CO-SLED (Yang et al. 2017), and for this reason the resulting value of  $L'_{\text{CO}(1-0)} \sim 1.6 \times 10^{10} \text{ K km s}^{-1} \text{ pc}^2$  is considered an upper limit. This estimate is consistent with the value of  $L'_{\text{CO}(1-0)} \sim 1.5 \times 10^{10}$  that was found by Harris et al. (2012), by adopting an indicative magnification factor of 10. We then compute the molecular gas mass by assuming two different values of  $\alpha_{\text{CO}} = 0.8$ –4.6. The value of  $\alpha = 0.8$  is calibrated from local ULIRGs with supersolar metallicity (Downes & Solomon 1998), while the higher value is calibrated from the Milky Way (Solomon & Barrett 1991).

The molecular gas content can also be estimated by means of the empirical calibration (Scoville et al. 2017) as  $\alpha \equiv < L_{\nu 850\mu\text{m}}/M_{\text{gas}} > = 6.7 \pm 1.7 \times 10^{19} \text{ erg s}^{-1} \text{ Hz}^{-1} M_{\odot}^{-1}$ .

Finally, we convert the dust content into gas, by assuming a variable gas-to-dust ratio of  $\delta_{\text{GDR}} = 30$ –92, referring to the typical solar and supersolar metallicities, following Magdis et al. (2012) and Fujimoto et al. (2022). The values obtained for the molecular gas masses are reported in Table 6. For consistency, we adopt the dust mass value inferred from CIGALE, but it is worth checking how the dust opacity could affect our results. However, we caution the reader against deriving the dust mass through the effective dust temperatures inferred from a single-temperature MBB, as this estimate does not reflect the actual dust content of the ISM (see, e.g., Scoville et al. 2016). We compute the temperature-weighted dust masses in the optically thick regime, by adopting the value of  $T_{\text{dust,thick}}$  obtained in Section 5.1. We infer  $\log M_{\text{dust,thick}} = 8.7 \pm 0.05 M_{\odot}$ , which is  $\sim 2.3$  times lower than the CIGALE estimate, and would result in a gas mass range of  $\log M_{\text{gas,GDR}} \sim (10.2\text{--}10.7) M_{\odot}$ .

The stellar mass estimate that was output from the SED fitting must be considered an upper limit. Indeed, given the lack of a clear detection in the NIR images, it is not possible to correctly estimate the contribution coming from the lens (see Section 3.3 for a further discussion). Moreover, the dark nature of this object hinders a complete sampling of the optical and NIR parts of the SED. Aside from the value reported in Table 5, we compute the stellar mass by assuming a typical stellar-to-dust mass ratio of  $\delta_{\text{SDR}} \approx 100$ , obtaining a value of  $M_{*}^{\text{STD}} \sim 1.1 \times 10^{11} M_{\odot}$ , which is in agreement with the SED fitting estimate.

### 5.3. Morphology and ISM Properties of J1135

From the reconstructed continuum originating from the dust (Figure 6), a clear “clumpy” double-peaked structure is visible. First, we compare the effective radii inferred from the dust continuum at different wavelengths. Excluding the lower-angular resolution reconstruction at 1.3 mm (band 6), the most resolved 0.64 and 1.0 mm emissions do not show particular differences in their spatial extensions that are ascribable to a dust temperature gradient, even though further observations are needed in order to explore this possibility. In Figure 13, we then overlap the SP maps reconstructed from our lens modeling for three different tracers. We show the C[II] and CO(8–7) line emission and the dust continuum at  $640 \mu\text{m}$ , the latter corresponding to the data set with the highest angular resolution. The first visible difference between the three emissions concerns their spatial extensions: while the C[II] and dust continuum occupy similar areas, the CO(8–7) is more extended. The size discrepancy is most likely associated with the differences in angular resolution of the respective data sets (see also the  $R_{\text{eff}}$  and  $\theta$  values reported in Table 4), rather than

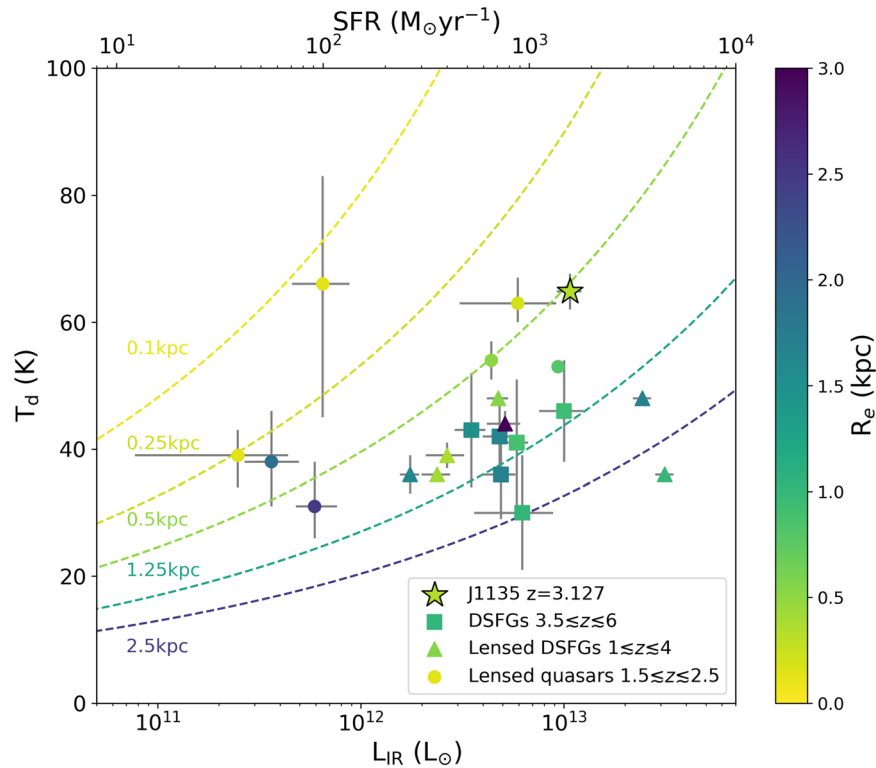


**Figure 12.** Dust temperature vs. IR luminosity, color coded according to effective radius. The dashed lines represent the modified Stefan–Boltzmann relation (Yan & Ma 2016); the circles show the sample of lensed quasars from Stacey et al. (2021); the triangles represent the sample of FIR-selected starbursts from Jin et al. (2022); and the squares show a sample of lensed DSFGs as selected by Herschel (Nayyeri et al. 2016; Dye et al. 2018)—the original values are taken from Table A.1 of Stacey et al. (2021). The star symbol shows J1135.

**Table 6**

Values for the Molecular Mass, Computed from Different Calibrators

Calibrator	$\log M_{\text{gas}} (M_{\odot})$
C[II]	$11.04 \pm 0.04$
CO(1–0)	$\lesssim (10.2–10.9)$
850 $\mu\text{m}$	$11.5 \pm 0.2$
$\alpha_{\text{GDR}}$	$(10.51–11.04) \pm 0.05$

being an intrinsic morphological difference. We also note that this difference is present in the dust continuum for the same data set as CO(8–7), i.e., band 6, where the estimated effective radii reach up to 1.1 kpc at  $3\sigma$ . This comparison shows a co-spatial emission for the dust continuum and C[II] line, even though the peaks are located at different positions. The clumpy structures also seem to be present in the reconstructed C[II] line emission, while they are not likely to be resolved for the CO(8–7) line, which extends in a more ellipsoidal profile.

From the average of the gas mass values reported in Section 5.2, we estimate the depletion timescale as  $\tau_{\text{depl}} \simeq M_{\text{gas}}/\text{SFR} \simeq 10^8 \text{ yr}$ , which translates to a high SFE, reaching up to  $\sim 10^{-8} \text{ yr}^{-1}$ . Moreover, the inferred stellar mass implies a star formation burst duration of  $\tau_{\text{SFR}} \simeq M_{*}/\text{SFR} \simeq 10^8 \text{ yr}$ , which is indicative of a young galaxy offset from the main-sequence locus of star-forming galaxies at  $z \sim 3$  (Speagle et al. 2014).

Our results are consistent with the expectations reported in Vishwas et al. (2018), where the analysis of the Lyman continuum photons required to sustain the luminosity of the O[III] 88  $\mu\text{m}$  line pointed out the presence of young and massive stars ionizing the surrounding H II regions. The same

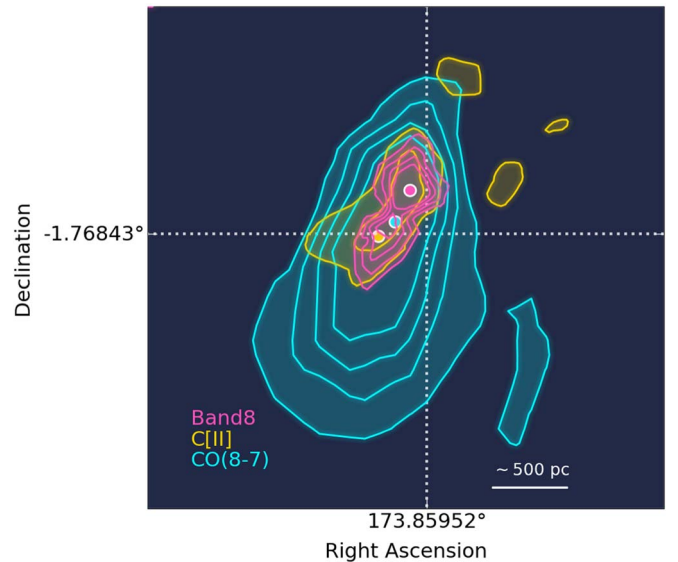


**Figure 13.** Comparison between the source-reconstructed emissions of the ALMA continuum at 640  $\mu\text{m}$  and the spectral emissions of the CO(8–7) and C[II] lines. The contours are displayed at  $9\sigma$ ,  $7\sigma$ ,  $5\sigma$ , and  $3\sigma$ , while the filled circles represent the positions of the peaks for each emission.

authors found no significant AGN contribution from the SED analysis, consistent with what we infer from the IRRC ( $q_{\text{IR}} \approx 2.8$ ), which is indicative of a star formation–dominated object. However, it should be pointed out that in the absence of a good sampling of the MIR part of the SED, the presence of the AGN in J1135 is still arguable. Moreover, the CO(8–7) line, associated with high transitions, can point toward the

presence of large amounts of energy that are linked with activity from a heavily dust-embedded central nucleus, as well as a strong star formation activity.

The hypothesis of J1135 being a compact starburst is also supported by the source reconstruction of the highest-angular resolution ALMA dust continuum emission at 640  $\mu\text{m}$  and 1.1 mm, shown in Figure 6, where the effective radius reaches an average value of  $\sim 350$  pc.

We now focus on the properties of the C[II] line of J1135. The C[II] line is a fine-structure line that predominantly originates from high- $z$  photon-dominated regions and is typically used as a cool interstellar gas tracer as well as an SFR estimator (see Casey et al. 2014 for a review). A well-known deficit in the C[II]/FIR ratio is observed in both nearby (e.g., Luhman et al. 2003; Diaz-Santos et al. 2017; Smith et al. 2017) and high-redshift star-forming galaxies (Stacey et al. 2010; Gullberg et al. 2015). This drop is found to reach very low values ( $L_{\text{C[II]}}/L_{\text{IR}} \approx 10^{-4}$ ) in spatially resolved studies (e.g., Gullberg et al. 2015; Lagache et al. 2018; Rybak et al. 2019). For J1135, we infer a C[II]/IR ratio of  $L_{\text{C[II]}}/L_{\text{IR}} \approx 5.4 \times 10^{-4}$ . Similar values are found for other strongly lensed galaxies among the H-ATLAS sample. For example, Rybak et al. (2020) reported a deficit down to  $\sim 3 \times 10^{-4}$  for spatially resolved ALMA data of SDP.81 at  $z = 3.042$  (Dye et al. 2015; Hatsukade et al. 2015; Partnership et al. 2015; Rybak et al. 2015a, 2015b; Swinbank et al. 2015; Tamura et al. 2015; Hezaveh et al. 2016). Lamarche et al. (2018) found similar values ( $\sim 2 \times 10^{-4}$ ) for SDP.11 at  $z = 1.7$ , even though our galaxy shows a more compact morphology in the C[II] emission with respect to other objects. We compute the star formation surface density by assuming  $\rho_{\text{SFR}} = 0.5 \times \frac{\text{SFR}}{\pi R_{\text{eff},5\sigma}^2}$  (Stacey et al. 2021), where  $R_{\text{eff},5\sigma}$  is the average of the effective radii of the  $5\sigma$  continuum dust emission at 640  $\mu\text{m}$  and 1.1 mm reported in Table 4. We infer a value of  $\rho_{\text{SFR}} \sim 1200 M_{\odot} \text{ yr}^{-1} \text{ kpc}^{-2}$ , which is consistent with a galaxy being on the verge of the Eddington limit for a radiation pressure-supported starburst (Andrews & Thompson 2011; Simpson et al. 2015). This result is compatible with the possible explanation of the deficit being attributed to a lower increase of the C[II] emission with respect to the IR.

#### 5.4. Evolutionary Interpretation

By inspecting the HST/WFC3 image, we find no evidence for galaxy companions of J1135 within a radius of at least  $\sim 5''$ , corresponding to  $\sim 40$  kpc, although the detection of possible closer and fainter sources is hindered by the current data sensitivities and angular resolutions. Moreover, from the CO(8–7) reconstructed image and the C[II] first moment map, we find no clear evidence of a complex kinematic structure possibly associated with a merging event. With no further hints pointing toward this scenario, we are led to interpret the ISM conditions and physical properties discussed so far in the light of in situ galaxy formation scenarios (Lapi et al. 2014; Mancuso et al. 2016a, 2016b, 2017; Lapi et al. 2018; Pantoni et al. 2019). In particular, the properties of J1135 are consistent with a compaction phase (Barro et al. 2014; Ikarashi et al. 2015, 2017; Kocevski et al. 2017; Silverman et al. 2019; Valentino et al. 2020; Stacey et al. 2021; and see also Figure 3 in Lapi et al. 2018), in which the dust-enshrouded star formation activity increases at an almost constant rate in the inner regions of the galaxy where the stellar mass is being accumulated. At this stage, the in situ scenario envisages the galaxy as an off-main-

sequence object at an early evolutionary stage, which will eventually move toward the main-sequence locus as the stellar mass content increases. Finally, the star formation will either progressively decrease, as the galaxy exhausts its gas reservoir, or it will be abruptly stopped by the action of the feedback from an AGN (Mancuso et al. 2016a, 2017).

## 6. Summary and Conclusions

In this work, we have investigated the nature of the strongly lensed galaxy HATLASJ113526.2-01460 (namely, J1135) at redshift  $z \approx 3.1$ , discovered by the Herschel satellite in the GAMA 12th field of the H-ATLAS survey. We have performed detailed lens modeling and reconstructed the source morphology in three different (sub)mm continuum bands, as well as in the spectral emission of the C[II] and CO(8–7) lines. We have also exploited a wealth of ancillary photometric data to perform broadband SED fitting and retrieve intrinsic (i.e., corrected for magnification) physical properties. Our main findings are summarized below:

1. The lens modeling indicates that the foreground lens is constituted by a (likely elliptical) galaxy with mass  $\gtrsim 10^{11} M_{\odot}$  at  $z \gtrsim 1.5$ , while the source is found to be an optical/NIR-dark dusty star-forming galaxy whose (sub)mm continuum and line emissions are amplified by factors  $\mu \sim 6\text{--}13$ .
2. The emission of J1135 is extremely compact, with sizes  $\lesssim 0.5$  kpc for the star-forming region and the most resolved gas component, and no clear evidence of strong rotation or ongoing merging events.
3. J1135 features a very high SFR  $\gtrsim 10^3 M_{\odot} \text{ yr}^{-1}$ , which, given the compact sizes, is on the verge of the Eddington limit for starbursts. The radio luminosity at 6 cm, from the available EVLA observations, is consistent with the star formation activity, such that no significant contribution from a central AGN is emerging (see also Vishwas et al. 2018).
4. J1135 is found to be extremely rich in gas  $\sim 10^{11} M_{\odot}$  and dust  $\gtrsim 10^9 M_{\odot}$ . The stellar content  $\lesssim 10^{11} M_{\odot}$  places J1135 well above the main sequence of star-forming galaxies, indicating that the starburst is rather young, with an estimated age  $\sim 10^8$  yr, and that the stellar mass should at least double before star formation is quenched.
5. The properties of J1135 can be consistently explained in terms of in situ galaxy formation and evolution scenarios as being typical of a rather young dusty star-forming galaxy that is caught in the compaction phase.

In the near future, observations coming from the James Webb Space Telescope will be crucial for shedding further light on the nature of this obscured object and its foreground lens in the NIR and MIR regimes. Moreover, X-ray follow-ups, coupled with the available ALMA data, will be required to establish the presence of the dust-enshrouded AGN and to better investigate the interplay between star formation and nuclear activity (Massardi et al. 2018).

This paper makes use of the following ALMA data: 2016.1.01371, 2017.1.01694.S, and 2018.1.00861.S. ALMA is a partnership of ESO (representing its member states), NSF (USA), and NINS (Japan), together with NRC (Canada), MOST and ASIAA (Taiwan), and KASI (Republic of Korea),

in cooperation with the Republic of Chile. The Joint ALMA Observatory is operated by ESO, AUI/NRAO, and NAOJ. We acknowledge financial support from the grant PRIN MIUR 2017 prot. 20173ML3WW 001 and 002, “Opening the ALMA window on the cosmic evolution of gas, stars, and super-massive black holes.” A.L. is supported by the EU H2020-MSCA-ITN-2019 project 860744 “BiD4BEST: Big Data applications for black hole Evolution STudies.” We acknowledge the anonymous referee for the useful comments.

*Software:* `astropy` (Astropy Collaboration 2013, 2018), CASA (v4.7.2; McMullin et al. 2007), `PyNUFFT` (Lin 2018), `PyLops` (Ravasi & Vasconcelos 2020), `PyAutoLens` (Nightingale et al. 2018, 2021), `CIGALE` (Boquien et al. 2019).

The HST data used in this paper can be found in MAST: [10.17909/zhns-ey90](https://archive.stsci.edu/hst/observing/10.17909/zhns-ey90).

The Spitzer data can be found in: [10.26131/IRSA543](https://irsa.ipac.caltech.edu/data/SPITZER/IRSA/10.26131/IRSA543).

The WISE data are available in: [10.26131/IRSA1](https://irsa.ipac.caltech.edu/data/WISE/IRSA/10.26131/IRSA1).

## Appendix

### Adapting the SLI Method to Interferometric Visibilities

The SLI formalism can also be extended to interferometry (Dye et al. 2018; Enia et al. 2018; Maresca et al. 2022), for modeling a set of visibility data, i.e., the result of a correlation of signals coming from an astrophysical source and collected by an antennae array, whose Fourier transform gives the source surface brightness distribution. Performing an inversion directly on the Fourier space (or  $uv$ -plane) circumvents the issue of dealing with artifacts and noise correlation arising in the image as a consequence of the poor sampling of the  $uv$ -plane.

Following a similar formalism with respect to the one used in Dye et al. (2018), we introduce the rectangular matrix  $f_{ij}$ , containing the fluxes of the  $i$ th pixel in the SP and the  $j$ th IP pixel, respectively. Analogously, the complex visibilities from the lensed image are collected in the rectangular matrix  $g_{ij}$ , which is the Fourier transform of the  $i$  source pixels in unit surface brightness computed at the  $j$ th visibility point in the  $uv$ -plane. For each  $j$ th visibility corresponding to the source pixel surface brightnesses  $s_i$ , the model visibility set can be described as  $\sum_i s_i g_{ij}$ .

Given a set of observed visibilities  $V_{\text{obs}}$ , the merit function can be described as:

$$G = \frac{1}{2} \chi^2 = \frac{1}{2} \sum_{j=1}^J \left( \frac{\left| \sum_{i=1}^I s_i g_{ij} - V_{\text{obs},j} \right|^2}{\sigma_j^2} \right) + \lambda \frac{1}{2} \mathbf{S}^T \mathbf{H} \mathbf{S}, \quad (\text{A1})$$










computed over a total of  $I$  Delaunay pixels and  $J$  visibilities.  $\sigma_j$  are the  $1\sigma$  uncertainties on the observed visibilities, rescaled by adopting the CASA task `statwt` to match their absolute value. The last term in the expression describes the regularization, where  $\lambda$  is a constant determining the strength of the regularization and  $\mathbf{H}$  is the regularization matrix. The values  $s_i$ , represented by the vector  $\mathbf{S}$ , which best reproduces the observed IP visibilities, can therefore be derived by minimizing the merit function  $G$ . The solution to this linear problem is given by:

$$\mathbf{S} = [\mathbf{F} + \lambda \mathbf{H}]^{-1} \mathbf{D}, \quad (\text{A2})$$

where  $\mathbf{F}$  and  $\mathbf{D}$  are the matrices  $F_{ij} = \sum_{n=1}^J (g_{in}^{\text{R}} g_{jn}^{\text{R}} + g_{in}^{\text{I}} g_{jn}^{\text{I}} / \sigma_n^2)$  and  $D_i = \sum_{n=1}^J (g_{in}^{\text{R}} V_n^{\text{R}} + g_{in}^{\text{I}} V_n^{\text{I}} / \sigma_n^2)$ , respectively.

For a fixed-mass model, the IP pixels are traced back to the SP and grouped together by means of a k-clustering algorithm, which compares each source pixel with its neighbors sharing a direct vertex. This procedure results in new SP centers, which are used to trace a Delaunay grid. When dealing with a large number of visibilities, the computational efficiency and memory costs are greatly improved by using the nonuniform Fast Fourier Transform algorithm, implemented in `PyAutoLens`, by exploiting the `PyNUFFT` (Lin 2018) library and the linear algebra package `PyLops` (Ravasi & Vasconcelos 2020).

## ORCID iDs

Marika Giulietti  <https://orcid.org/0000-0002-1847-4496>  
 Andrea Lapi  <https://orcid.org/0000-0002-4882-1735>  
 Marcella Massardi  <https://orcid.org/0000-0002-0375-8330>  
 Meriem Behiri  <https://orcid.org/0000-0002-6444-8547>  
 Martina Torsello  <https://orcid.org/0000-0001-9301-5209>  
 Quirino D’Amato  <https://orcid.org/0000-0002-9948-0897>  
 Tommaso Ronconi  <https://orcid.org/0000-0002-3515-6801>  
 Francesca Perrotta  <https://orcid.org/0000-0001-9808-0843>  
 Alessandro Bressan  <https://orcid.org/0000-0002-7922-8440>

## References

- Aihara, H., Armstrong, R., Bickerton, S., et al. 2018, *PASJ*, 70, S8  
 Aihara, H., AlSayyad, Y., Ando, M., et al. 2022, *PASJ*, 74, 247  
 Alcalde Pampiega, B., Perez-Gonzalez, P. G., Barro, G., et al. 2019, *ApJ*, 876, 135  
 Andreani, P., Retana-Montenegro, E., Zhang, Z.-Y., et al. 2018, *A&A*, 615, A142  
 Andrews, B. H., & Thompson, T. A. 2011, *ApJ*, 727, 97  
 Aravena, M., Decarli, R., Walter, F., et al. 2016, *ApJ*, 833, 71  
 Astropy Collaboration, Price-Whelan, A. M., Sipőcz, B. M., et al. 2018, *AJ*, 156, 123  
 Astropy Collaboration, Robitaille, T. P., Tollerud, E. J., et al. 2013, *A&A*, 558, A33  
 Bakx, T. J. L. C., Eales, S. A., Negrello, M., et al. 2018, *MNRAS*, 473, 1751  
 Barro, G., Faber, S. M., Perez-Gonzalez, P. G., et al. 2014, *ApJ*, 791, 52  
 Becker, R. H., White, R. L., & Helfand, D. J. 1995, *ApJ*, 450, 559  
 Berta, S., Lutz, D., Genzel, R., Förster-Schreiber, N. M., & Tacconi, L. J. 2016, *A&A*, 587, A73  
 Blain, A. W. 1996, *MNRAS*, 283, 1340  
 Boquien, M., Burgarella, D., Roehly, Y., et al. 2019, *A&A*, 622, A103  
 Bruzual, G., & Charlot, S. 2003, *MNRAS*, 344, 1000  
 Bussmann, R. S., Perez-Fournon, I., Amber, S., et al. 2013, *ApJ*, 779, 25  
 Calanog, J. A., Fu, H., Cooray, A., et al. 2014, *ApJ*, 797, 138  
 Carilli, C. L., & Walter, F. 2013, *ARA&A*, 51, 105  
 Casey, C. M., Narayanan, D., & Cooray, A. 2014, *PhR*, 541, 45  
 Chabrier, G. 2003, *PASP*, 115, 763  
 Charlot, S., & Fall, S. M. 2000, *ApJ*, 539, 718  
 Cortzen, I., Magdis, G. E., Valentino, F., et al. 2020, *A&A*, 634, L14  
 de Jong, J. T. A., Kuijken, K., Applegate, D., et al. 2013, *Msngr*, 154, 44  
 Diaz-Santos, T., Armus, L., Charmandaris, V., et al. 2017, *ApJ*, 846, 32  
 Downes, D., & Solomon, P. M. 1998, *ApJ*, 507, 615  
 Draine, B. T. 2011, *Physics of the Interstellar and Intergalactic Medium* (Princeton, NJ: Princeton Univ. Press)  
 Draine, B. T., & Li, A. 2007, *ApJ*, 657, 810  
 Draine, B. T., Aniano, G., Krause, O., et al. 2014, *ApJ*, 780, 172  
 Dudzevičiūtė, U., Smail, I., Swinbank, A., et al. 2020, *MNRAS*, 494, 3828  
 Dunlop, J. S., McLure, R. J., Biggs, A. D., et al. 2017, *MNRAS*, 466, 861  
 Dye, S., Furlanetto, C., Swinbank, A. M., et al. 2015, *MNRAS*, 452, 2258  
 Dye, S., Furlanetto, C., Dunne, L., et al. 2018, *MNRAS*, 476, 4383  
 Dye, S., Eales, S. A., Gomez, H. L., et al. 2022, *MNRAS*, 510, 3734  
 Eales, S., Dunne, L., Clements, D., et al. 2010, *PASP*, 122, 499  
 Edge, A., Sutherland, W., Kuijken, K., et al. 2013, *Msngr*, 154, 32  
 Enia, A., Negrello, M., Gurwell, M., et al. 2018, *MNRAS*, 475, 3467  
 Enia, A., Talia, M., Pozzi, F., et al. 2022, *ApJ*, 927, 204  
 Franco, M., Elbaz, D., Bethermin, M., et al. 2018, *A&A*, 620, A152

- Fujimoto, S., Brammer, G. B., Watson, D., et al. 2022, *Natur*, 604, 261
- Gruppioni, C., Béthermin, M., Loiacono, F., et al. 2020, *A&A*, 643, A8
- Gullberg, B., De Breuck, C., Vieira, J. D., et al. 2015, *MNRAS*, 449, 2883
- Harris, A. I., Baker, A. J., Frayer, D. T., et al. 2012, *ApJ*, 752, 152
- Hatsukade, B., Tamura, Y., Iono, D., et al. 2015, *PASJ*, 67, 93
- Hatsukade, B., Kohno, K., Yamaguchi, Y., et al. 2018, *PASJ*, 70, 105
- Hezaveh, Y. D., Dalal, N., Marrone, D. P., et al. 2016, *ApJ*, 823, 37
- Ikarashi, S., Ivison, R. J., Caputi, K. I., et al. 2015, *ApJ*, 810, 133
- Ikarashi, S., Caputi, K. I., Ohta, K., et al. 2017, *ApJL*, 849, L36
- Jin, S., Daddi, E., Magdis, G. E., et al. 2019, *ApJ*, 887, 144
- Jin, S., Daddi, E., Magdis, G. E., et al. 2022, *A&A*, 665, A3
- Kocevski, D. D., Barro, G., Faber, S. M., et al. 2017, *ApJ*, 846, 112
- Kormann, R., Schneider, P., & Bartelmann, M. 1994, *A&A*, 284, 285
- Lagache, G., Cousin, M., & Chatzikos, M. 2018, *A&A*, 609, A130
- Lamarche, C., Verma, A., Vishwas, A., et al. 2018, *ApJ*, 867, 140
- Lapi, A., Negrello, M., Gonzalez-Nuevo, J., et al. 2012, *ApJ*, 755, 46
- Lapi, A., Raimundo, S., Aversa, R., et al. 2014, *ApJ*, 782, 69
- Lapi, A., Pantoni, L., Zanisi, L., et al. 2018, *ApJ*, 857, 22
- Lawrence, A., Warren, S. J., Almaini, O., et al. 2007, *MNRAS*, 379, 1599
- Lin, J.-M. 2018, *J. Imaging*, 4, 51
- Luhman, M. L., Satyapal, S., Fischer, J., et al. 2003, *ApJ*, 594, 758
- Ma, B., Cooray, A., Calanog, J. A., et al. 2015, *ApJ*, 814, 17
- Maddox, S. J., Valiante, E., Cigan, P., et al. 2018, *ApJS*, 236, 30
- Magdis, G. E., Daddi, E., Béthermin, M., et al. 2012, *ApJ*, 760, 6
- Mancuso, C., Lapi, A., Prandoni, I., et al. 2017, *ApJ*, 842, 95
- Mancuso, C., Lapi, A., Shi, J., et al. 2016a, *ApJ*, 833, 152
- Mancuso, C., Lapi, A., Shi, J., et al. 2016b, *ApJ*, 823, 128
- Maresca, J., Dye, S., Amvrosiadis, A., et al. 2022, *MNRAS*, 512, 2426
- Marrone, D. P., Spilker, J. S., Hayward, C. C., et al. 2018, *Natur*, 553, 51
- Massardi, M., Enia, A. F. M., Negrello, M., et al. 2018, *A&A*, 610, A53
- McMullin, J. P., Waters, B., Schiebel, D., Young, W., & Golap, K. 2007, in ASP Conf. Ser. 376, *Astronomical Data Analysis Software and Systems XVI*, ed. R. A. Shaw, F. Hill, & D. J. Bell (San Francisco, CA: ASP), 127
- Nayyeri, H., Keele, M., Cooray, A., et al. 2016, *ApJ*, 823, 17
- Negrello, M., Amber, S., Amvrosiadis, A., et al. 2017, *MNRAS*, 465, 3558
- Negrello, M., Hopwood, R., De Zotti, G., et al. 2010, *Sci*, 330, 800
- Negrello, M., Hopwood, R., Dye, S., et al. 2014, *MNRAS*, 440, 1999
- Nightingale, J., Hayes, R., Kelly, A., et al. 2021, *JOSS*, 6, 2825
- Nightingale, J. W., & Dye, S. 2015, *MNRAS*, 452, 2940
- Nightingale, J. W., Dye, S., & Massey, R. J. 2018, *MNRAS*, 478, 4738
- Oliver, S. J., Bock, J., Altieri, B., et al. 2012, *MNRAS*, 424, 1614
- Pantoni, L., Lapi, A., Massardi, M., Goswami, S., & Danese, L. 2019, *ApJ*, 880, 129
- Pantoni, L., Massardi, M., Lapi, A., et al. 2021, *MNRAS*, 507, 3998
- Partnership, A., Vlahakis, C., Hunter, T. R., et al. 2015, *ApJL*, 808, L4
- Planck Collaboration, Aghanim, N., Akrami, Y., et al. 2020, *A&A*, 641, A6
- Polletta, M., Tajer, M., Maraschi, L., et al. 2007, *ApJ*, 663, 81
- Ravasi, M., & Vasconcelos, I. 2020, *SoftX*, 11, 100361
- Riechers, D. A., Bradford, C. M., Clements, D. L., et al. 2013, *Natur*, 496, 329
- Riechers, D. A., Hodge, J. A., Pavesi, R., et al. 2020, *ApJ*, 895, 81
- Rizzo, F., Vegetti, S., Fraternali, F., Stacey, H. R., & Powell, D. 2021, *MNRAS*, 507, 3952
- Rybak, M., Hodge, J. A., Vegetti, S., et al. 2020, *MNRAS*, 494, 5542
- Rybak, M., McKean, J. P., Vegetti, S., Andreani, P., & White, S. D. M. 2015a, *MNRAS*, 451, L40
- Rybak, M., Vegetti, S., McKean, J. P., Andreani, P., & White, S. D. M. 2015b, *MNRAS*, 453, L26
- Rybak, M., Rivera, G. C., Hodge, J. A., et al. 2019, *ApJ*, 876, 112
- Scoville, N., Sheth, K., Aussel, H., et al. 2016, *ApJ*, 820, 83
- Scoville, N., Murchikova, L., Walter, F., et al. 2017, *ApJ*, 836, 66
- Scoville, N., Lee, N., Bout, P. V., et al. 2017, *ApJ*, 837, 150
- Shu, X., Yang, L., Liu, D., et al. 2022, *ApJ*, 926, 155
- Silverman, J. D., Treu, T., Ding, X., et al. 2019, *ApJL*, 887, L5
- Simpson, J. M., Swinbank, A. M., Smail, I., et al. 2014, *ApJ*, 788, 125
- Simpson, J. M., Smail, I., Swinbank, A. M., et al. 2015, *ApJ*, 799, 81
- Simpson, J. M., Smail, I., Swinbank, A. M., et al. 2017, *ApJ*, 839, 58
- Simpson, J. M., Smail, I., Dudzevičiūtė, U., et al. 2020, *MNRAS*, 495, 3409
- Smith, J. D. T., Croxall, K., Draine, B., et al. 2017, *ApJ*, 834, 5
- Solomon, P. M., & Barrett, J. W. 1991, in IAU Symp. 146, *Dynamics of Galaxies and Their Molecular Cloud Distributions*, ed. Cloud (Dordrecht: Kluwer), 235
- Speagle, J. S., Steinhardt, C. L., Capak, P. L., & Silverman, J. D. 2014, *ApJS*, 214, 15
- Speagle, J. S. 2020, *MNRAS*, 493, 3132
- Spilker, J. S., Marrone, D. P., Aravena, M., et al. 2016, *ApJ*, 826, 112
- Stacey, G. J., Hailey-Dunsheath, S., Ferkinhoff, C., et al. 2010, *ApJ*, 724, 957
- Stacey, H. R., McKean, J. P., Powell, D. M., et al. 2021, *MNRAS*, 500, 3667
- Swinbank, A. M., Dye, S., Nightingale, J. W., et al. 2015, *ApJL*, 806, L17
- Talia, M., Cimatti, A., Giulietti, M., et al. 2021, *ApJ*, 909, 23
- Tamura, Y., Oguri, M., Iono, D., et al. 2015, *PASJ*, 67, 72
- Valentino, F., Daddi, E., Puglisi, A., et al. 2020, *A&A*, 641, A155
- Valiante, E., Smith, M. W. L., Eales, S., et al. 2016, *MNRAS*, 462, 3146
- Viero, M. P., Asboth, V., Roseboom, I. G., et al. 2014, *ApJS*, 210, 22
- Vishwas, A., Ferkinhoff, C., Nikola, T., et al. 2018, *ApJ*, 856, 174
- Walter, F., Decarli, R., Aravena, M., et al. 2016, *ApJ*, 833, 67
- Wang, T., Elbaz, D., Schreiber, C., et al. 2016, *ApJ*, 816, 84
- Wang, T., Schreiber, C., Elbaz, D., et al. 2019, *Natur*, 572, 211
- Ward, B. A., Eales, S. A., Pons, E., et al. 2022, *MNRAS*, 510, 2261
- Wardlow, J. L., Cooray, A., De Bernardis, F., et al. 2013, *ApJ*, 762, 59
- Warren, S. J., & Dye, S. 2003, *ApJ*, 590, 673
- Williams, C. C., Labbe, I., Spilker, J., et al. 2019, *ApJ*, 884, 154
- Wright, E. L., Eisenhardt, P. R. M., Mainzer, A. K., et al. 2010, *AJ*, 140, 1868
- Yan, H., & Ma, Z. 2016, *ApJL*, 820, L16
- Yang, C., Omont, A., Beelen, A., et al. 2017, *A&A*, 608, A144
- Zanella, A., Daddi, E., Magdis, G., et al. 2018, *MNRAS*, 481, 1976